

REPORT DOCUMENTATION PAGE				Form Approved OMB No. 0704-0188	
1a. REPORT SECURITY CLASSIFICATION UNCLASSIFIED			1b. RESTRICTIVE MARKINGS		
2a. SECURITY CLASSIFICATION AUTHORITY			3. DISTRIBUTION / AVAILABILITY OF REPORT Approved for public release; distribution unlimited.		
2b. DECLASSIFICATION / DOWNGRADING SCHEDULE					
4. PERFORMING ORGANIZATION REPORT NUMBER(S) NRL Memorandum Report 6075			5. MONITORING ORGANIZATION REPORT NUMBER(S)		
6a. NAME OF PERFORMING ORGANIZATION Naval Research Laboratory		6b. OFFICE SYMBOL (If applicable) Code 4430		7a. NAME OF MONITORING ORGANIZATION Office of Naval Research	
6c. ADDRESS (City, State, and ZIP Code) Washington, DC 20375-5000			7b. ADDRESS (City, State, and ZIP Code) Arlington, VA 22217		
8a. NAME OF FUNDING / SPONSORING ORGANIZATION Office of Naval Research		8b. OFFICE SYMBOL (If applicable)		9. PROCUREMENT INSTRUMENT IDENTIFICATION NUMBER	
8c. ADDRESS (City, State, and ZIP Code) Arlington, VA 22217			10. SOURCE OF FUNDING NUMBERS		
			PROGRAM ELEMENT NO. 61153N	PROJECT NO.	TASK NO. RR023- 01-001
			WORK UNIT ACCESSION NO. DN157-111		
11. TITLE (Include Security Classification) Calculations of the Turbulent Wake Behind a Slender Self-Propelled Double-Body and Comparisons with Experiment					
12. PERSONAL AUTHOR(S) Swean, T.F., Jr.					
13a. TYPE OF REPORT Interim		13b. TIME COVERED FROM 1/1/87 TO present		14. DATE OF REPORT (Year, Month, Day) 1987 October 6	
				15. PAGE COUNT 45	
16. SUPPLEMENTARY NOTATION					
17. COSATI CODES			18. SUBJECT TERMS (Continue on reverse if necessary and identify by block number)		
FIELD	GROUP	SUB-GROUP			
			Turbulent wake Self-propelled		
			Finite-element		
19. ABSTRACT (Continue on reverse if necessary and identify by block number)					
<p>The parabolic, incompressible, time-averaged Navier-Stokes equations together with a two-equation, (K, ϵ), model of turbulence are used to numerically simulate the wake downstream of a slender double-body. The equations are solved using the finite-element method and the results are compared to experimental data for both unpropelled and self-propelled configurations. With the exception of certain localized phenomena, the calculations and experiments are found to be in good agreement for the mean velocity components, the turbulence kinetic energy, and the Reynolds shear stresses. The noteworthy exception for the unpropelled configuration is the prediction of a rather strong region of production of turbulence in the near wake which is not evident in the data. The simulation of the self-propelled wake is in good agreement with the data for the mean velocity components. There is also acceptable agreement for the turbulence parameters over most of the wake cross-section except near the radius of the propeller tips. Severe qualitative and quantitative discrepancies in this region are possibly due to the presence of periodic components in the data.</p>					
20. DISTRIBUTION / AVAILABILITY OF ABSTRACT <input checked="" type="checkbox"/> UNCLASSIFIED/UNLIMITED <input type="checkbox"/> SAME AS RPT. <input type="checkbox"/> DTIC USERS			21. ABSTRACT SECURITY CLASSIFICATION UNCLASSIFIED		
22a. NAME OF RESPONSIBLE INDIVIDUAL Thomas F. Swean, Jr.			22b. TELEPHONE (Include Area Code) (202) 767-2114		22c. OFFICE SYMBOL Code 4430

Naval Research Laboratory

Washington, DC 20375-5000

LIBRARY
RESEARCH REPORTS DIVISION
NAVAL POSTGRADUATE SCHOOL
MONTEREY, CALIFORNIA 93940



NRL-Memorandum Report-6075

Calculations of the Turbulent Wake Behind A Slender Self-Propelled Double-Body and Comparisons with Experiment

✓ THOMAS F. SWEAN, JR.

*Center for Hydrodynamic Developments
Laboratory for Computational Physics and Fluid Dynamics*

L October 6, 1987

CONTENTS

1. INTRODUCTION	1
2. TEST CASES	2
3. PREDICTION MODEL	3
4. RESULTS AND COMPARISONS WITH EXPERIMENTAL DATA	9
5. SUMMARY	14
6. ACKNOWLEDGEMENTS	16
7. REFERENCES	17

CALCULATIONS OF THE TURBULENT WAKE BEHIND A SLENDER SELF-PROPELLED DOUBLE-BODY AND COMPARISONS WITH EXPERIMENT

1. INTRODUCTION

The turbulent flow field in the wake of a surface ship is the result of a complex combination of drag and lift elements from the hull and control surfaces together with swirl and thrust components from the propulsion system; all of which interact with each other, with the free surface and with any ambient flow. Beyond a relatively short developmental region the three-dimensional wake becomes dominated by the axial velocity component and the mathematical representation of the flow field assumes a parabolic character. Such a flow provides an exacting test of the generality of phenomenological turbulence models and calculation procedures.

A treatment of the very near-body (elliptic) region of swirling wake flows has been given by Schetz and Favin (1977, 1979). Their analyses considered the unsteady, axisymmetric (with nonzero peripheral velocity), time-averaged Navier-Stokes equations. The turbulence model was a one-equation model based on an integrated turbulence kinetic energy equation with an extension to represent the effects of swirl. Detailed comparisons with wind tunnel measurements in the near-wake region show a good prediction of the axial velocity but an underprediction of the swirl level. Swanson and Schetz (1975) present numerical simulations of the far-wake behavior behind a self-propelled body. Their model considered the streamwise momentum equation together with a one-equation turbulence model describing the turbulence kinetic energy. Their results show fairly good agreement between experiment and computation for the streamwise evolutions of maximum axial velocity and maximum shear stress. Their numerical procedure did not include the effects of swirl which had decayed to low levels in the range of X/D which they considered.

The present effort was undertaken to assess the success with which the parabolic Navier-Stokes equations together with a state-of-the-art two-equation model of turbulence may be used to predict the development of a strongly swirling wake downstream of a self-propelled body. The experiments of Mitra, Neu, and Schetz (1985, 1986), believed to be the most recent studies of self-propelled wake flows in the open literature, have been selected as a data base. In the following sections brief descriptions of the above experiments and the computational methods are given.

2. TEST CASES

Several experiments have recently been completed at Virginia Polytechnic Institute and State University which document the turbulent wake downstream of an axisymmetric slender body connected by a long thin flat plate strut to an image body (Mitra, Neu, and Schetz, 1985, 1986). A schematic of the experimental arrangement is shown in Fig. 1. The model consisted of two slender axisymmetric bodies connected in the vertical plane of symmetry by a flat plate strut. The image plane was one body diameter from the centerline of the lower axisymmetric body. The lower body of the model housed a strain gage balance which measured all six components of forces and moments acting on the lower body alone. These data were used to obtain the drag coefficient for the unpropelled experiments and to determine the self-propelled and over-thrusted conditions for the later experiments. The entire assembly was suspended from the ceiling of the Virginia Tech 6 ft by 6 ft closed return wind tunnel.

The first experiments were performed for the unpropelled model at a nominal Reynolds number (based on body diameter) of $Re_D = 6.0 \times 10^5$, which corresponds to a test section velocity of 210 ft/sec. Hot wire measurements were taken at three streamwise stations, $X/D = (0.042, 1.0, 33.0)$, of the mean velocity components, the turbulence intensities, the Reynolds stresses, and the static pressure. Thus, all the variables usually treated in the Reynolds averaged Navier-Stokes equations and K, ϵ formulations of turbulent flows were documented. At each station a measurement grid similar to that shown in Fig. 2 was used. The numbers in the figure refer to the measurement points. Several points were included along the positive Y/D axis and above the plane $Z/D = 1.0$ in order to monitor the symmetry of the flow field.

In the second set of experiments the model of Fig. 1 was fitted with counter-rotating three-bladed propellers (6 in diameter) constructed from model airplane propellers. The wind tunnel was operated at $Re_D = 4.5 \times 10^5$, (150 ft/sec). Measurements were taken as described above with the exceptions that the near-body measurement plane was moved downstream to $X/D = 0.208$ and the far-wake plane was moved upstream to $X/D = 28.0$. The measurements were performed for two different thrust conditions, at the self-propulsion point and at the 100% over-thrust point. Since the data from each of the thrusted investigations are qualitatively similar, the numerical simulations discussed in this report will consider only the drag and self-propelled experiments.

The above described experiments provide a significant contribution to the establishment of a well-documented data base with which to assess the accuracy of computational models. The experimental configuration is of particular engineering interest since it can be related to the flow in the wake of one of the submerged hulls of a SWATH type

ocean vehicle. The image body provides a symmetry plane which simulates the free surface under the "rigid lid" approximation which replaces the generally non-planar free surface by a fictitious plane free-slip boundary perpendicular to the gravity vector. The next section briefly describes the mathematical model and computational algorithm used to compute this flow field.

3. PREDICTION MODEL

Governing Equation System

It is assumed that the computational domain begins sufficiently far downstream of the body and propeller that the flow is governed by the steady, three-dimensional, time-averaged (in the turbulence sense) parabolic Navier-Stokes equations. The fundamental assumptions in obtaining the parabolic equations from the full Navier-Stokes system are that:

- 1) the axial velocity suffers no reversal,
- 2) diffusive transport processes in the axial direction are negligible, and
- 3) the overall elliptic character of the full Navier-stokes system is enforceable through the construction of a suitable pressure field with exterior flow boundary conditions.

For the flow situations considered in this study it is further assumed that density variations and fluctuations are negligible and that laminar diffusion is small compared to that due to turbulence.

With the above assumptions the appropriate equation set is (written on the cartesian coordinate system of Figs. 1 and 2),

continuity:

$$\frac{\partial \bar{U}}{\partial X} + \frac{\partial \bar{V}}{\partial Y} + \frac{\partial \bar{W}}{\partial Z} = 0, \quad (1)$$

axial momentum:

$$\bar{U} \frac{\partial \bar{U}}{\partial X} + \bar{V} \frac{\partial \bar{U}}{\partial Y} + \bar{W} \frac{\partial \bar{U}}{\partial Z} = -\frac{1}{\rho_\infty} \frac{\partial P}{\partial X} - \frac{\partial(\overline{u'v'})}{\partial Y} - \frac{\partial(\overline{u'w'})}{\partial Z}, \quad (2)$$

vertical momentum:

$$\bar{U} \frac{\partial \bar{W}}{\partial X} + \bar{V} \frac{\partial \bar{W}}{\partial Y} + \bar{W} \frac{\partial \bar{W}}{\partial Z} = -\frac{1}{\rho_\infty} \frac{\partial P}{\partial Z} - \frac{\partial(\overline{v'w'})}{\partial Y} - \frac{\partial(\overline{w'w'})}{\partial Z}, \quad (3)$$

cross-stream momentum:

$$\bar{U} \frac{\partial \bar{V}}{\partial X} + \bar{V} \frac{\partial \bar{V}}{\partial Y} + \bar{W} \frac{\partial \bar{V}}{\partial Z} = -\frac{1}{\rho_\infty} \frac{\partial P}{\partial Y} - \frac{\partial(\overline{v'v'})}{\partial Y} - \frac{\partial(\overline{v'w'})}{\partial Z}. \quad (4)$$

The variables appearing in the above equations have their usual interpretation in fluid mechanics, where capitalized dependent variables denote mean quantities and the lower case variables denote the Reynolds stresses.

In order to produce secondary flows in turbulent duct flows, the prediction procedure of Launder and Ying (1973) used an algebraic stress model developed from a degenerate form of the cross-flow plane Reynolds stress transport equation in which transport by convection and diffusion are neglected. By taking the dissipation of Reynolds stress to be locally isotropic and using the Hanjalic and Launder (1972) pressure-strain relationship, Launder and Ying reduced the differential transport equation to algebraic equations from which the cross-flow plane Reynolds stresses could be extracted. Gesner and Emery (1976) showed that the axial flow plane Reynolds stresses could also be extracted. Baker et al. (1979) has generalized the analysis of Gesner and Emery. With this generalization the kinematic Reynolds stresses appearing in Eqs. (2) through (4) are:

$$\overline{u'u'} = C_1 K - C_2 C_4 \frac{K^3}{\epsilon^2} \left(\left(\frac{\partial \bar{U}}{\partial Y} \right)^2 + \left(\frac{\partial \bar{U}}{\partial Z} \right)^2 \right) - 2C_4 \frac{K^2}{\epsilon} \left(\frac{\partial \bar{U}}{\partial X} \right), \quad (5)$$

$$\overline{v'v'} = C_3 K - C_2 C_4 \frac{K^3}{\epsilon^2} \left(\frac{\partial \bar{U}}{\partial Y} \right)^2 - 2C_4 \frac{K^2}{\epsilon} \left(\frac{\partial \bar{V}}{\partial Y} \right), \quad (6)$$

$$\overline{w'w'} = C_3 K - C_2 C_4 \frac{K^3}{\epsilon^2} \left(\frac{\partial \bar{U}}{\partial Z} \right)^2 - 2C_4 \frac{K^2}{\epsilon} \left(\frac{\partial \bar{W}}{\partial Z} \right), \quad (7)$$

$$\overline{u'v'} = -C_4 \frac{K^2}{\epsilon} \left(\frac{\partial \bar{U}}{\partial Y} \right) - C_2 C_4 \frac{K^3}{\epsilon^2} \left(\frac{\partial \bar{U}}{\partial Z} \left(\frac{\partial \bar{V}}{\partial Z} + \frac{\partial \bar{W}}{\partial Y} \right) - 2 \frac{\partial \bar{U}}{\partial Y} \frac{\partial \bar{W}}{\partial Z} \right), \quad (8)$$

$$\overline{u'w'} = -C_4 \frac{K^2}{\epsilon} \left(\frac{\partial \bar{U}}{\partial Z} \right) - C_2 C_4 \frac{K^3}{\epsilon^2} \left(\frac{\partial \bar{U}}{\partial Y} \left(\frac{\partial \bar{V}}{\partial Z} + \frac{\partial \bar{W}}{\partial Y} \right) - 2 \frac{\partial \bar{U}}{\partial Z} \frac{\partial \bar{V}}{\partial Y} \right), \quad (9)$$

$$\overline{v'w'} = -C_4 \frac{K^2}{\epsilon} \left(\frac{\partial \bar{V}}{\partial Z} + \frac{\partial \bar{W}}{\partial Y} \right) - C_2 C_4 \frac{K^3}{\epsilon^2} \left(\frac{\partial \bar{U}}{\partial Y} \frac{\partial \bar{U}}{\partial Z} \right). \quad (10)$$

In the above equations K is the turbulence kinetic energy and ϵ is its dissipation rate. These variables are calculated from the modelled transport equations

$$\overline{U} \frac{\partial K}{\partial X} + \overline{V} \frac{\partial K}{\partial Y} + \overline{W} \frac{\partial K}{\partial Z} = \frac{\partial}{\partial Y} \left(\frac{\nu_t}{\sigma_K} \frac{\partial K}{\partial Y} \right) + \frac{\partial}{\partial Z} \left(\frac{\nu_t}{\sigma_K} \frac{\partial K}{\partial Z} \right) + \mathcal{P} - \epsilon \quad (11)$$

and

$$\overline{U} \frac{\partial \epsilon}{\partial X} + \overline{V} \frac{\partial \epsilon}{\partial Y} + \overline{W} \frac{\partial \epsilon}{\partial Z} = \frac{\partial}{\partial Y} \left(\frac{\nu_t}{\sigma_\epsilon} \frac{\partial \epsilon}{\partial Y} \right) + \frac{\partial}{\partial Z} \left(\frac{\nu_t}{\sigma_\epsilon} \frac{\partial \epsilon}{\partial Z} \right) + C_{\epsilon_1} \mathcal{P} \frac{\epsilon}{K} - C_{\epsilon_2} \frac{\epsilon^2}{K}. \quad (12)$$

In Eqs. (11) and (12) the term \mathcal{P} is the mechanical production of kinetic energy,

$$\mathcal{P} = -\overline{u'v'} \frac{\partial \overline{U}}{\partial Y} - \overline{u'w'} \frac{\partial \overline{U}}{\partial Z} - \overline{v'w'} \left(\frac{\partial \overline{V}}{\partial Z} + \frac{\partial \overline{W}}{\partial Y} \right) - (\overline{v'v'} - \overline{u'u'}) \frac{\partial \overline{V}}{\partial Y} - (\overline{w'w'} - \overline{u'u'}) \frac{\partial \overline{W}}{\partial Z}$$

and the term ν_t is the turbulent kinematic viscosity,

$$\nu_t = C_4 \frac{K^2}{\epsilon}.$$

In order to be consistent with the aim of assessing the capability of the prediction procedure for computing self-propelled wake flows no attempt has been made to optimize the empirical constants. In its standard form the model contains the eight constants $\{C_1, C_2, C_3, C_4, \sigma_K, \sigma_\epsilon, C_{\epsilon_1}, C_{\epsilon_2}\}$ which take on the commonly accepted values $\{0.94, 0.067, 0.56, 0.068, 1.0, 1.3, 1.44, 1.92\}$.

Solution Procedure

In the present work the three-dimensional parabolic flow method of Baker (1983) is used to solve the governing equations. An exposition of the algorithm requires immense development of notation and, since the methodology is set forth in exacting detail in the above reference, it will only be summarized in this report. The method employs a finite-element marching procedure. The transverse plane is discretized into a number of sub-domains or finite elements. A discrete approximation of the governing equation system is written on these elements resulting in a system of ordinary differential equations written on the streamwise coordinate. This system is converted into a nonlinear algebraic equation system which is solved using a Newton iteration algorithm.

The evaluation of the pressure requires special mention. Baker (1983) recasts Eqs. (3) and (4) as a Poisson equation for pressure. The pressure that satisfies this Poisson equation consists of complementary and particular parts. The complementary field, P_c , is the solution to the homogeneous equation with specified Dirichlet conditions at boundaries where the freestream static pressure is known. The pressure in the axial momentum Eq. (2) is then identified as the complementary pressure, P_c . The particular pressure, P_p , is the solution to the full Poisson equation which vanishes at boundary locations where the complementary pressure is known. Elsewhere the normal gradient is specified via Eqs. (3) and (4) as appropriate. This pressure is used in the transverse momentum equations coupled via a penalty algorithm to Eq. (1) to enforce continuity.

In the experiments under consideration, the static pressure data reveal significant gradients in each of the crossplane coordinate directions as well as in the longitudinal direction between the first two planes. In order to numerically simulate this behavior fully it is necessary to solve the potential flow over the relatively complex double-body geometry. Rather than undertake that effort and in keeping with the goal of assessing the capability of the turbulence model to predict the wake evolution, the experimental data was used directly in Eq. (2) to specify the pressure gradient $\partial P_c / \partial X$. The particular pressure is, of course, free to conform to the solution and will influence the crossplane velocity components.

Boundary Conditions

The cross-sectional computational domain for the drag-body wake is that part of Fig. 2 bounded at the top, left, bottom, and right by the planes $Z/D = 1.0$, $Y/D = -1.5$, $Z/D = -1.5$, and $Y/D = 0.0$ respectively. The top and right boundaries are planes of symmetry while the left and bottom boundaries are considered to be in the free stream. At symmetry planes the velocity component normal to the symmetry boundary is zero and the normal gradients to the boundary of the other dependent variables are zero. The freestream boundary conditions are vanishing normal gradients for all dependent variables.

For the self-propelled experiments the symmetry about the plane $Y/D = 0.0$ is destroyed by the convective action of the propeller swirl, particularly when the swirling wake encounters the essentially two-dimensional wake of the strut. In this case the right boundary of the computational domain is moved to $Y/D = 1.5$ and freestream boundary conditions are there applied. Symmetry conditions are applied in the horizontal plane $Z/D = 1.0$ and freestream conditions are used at the other three boundaries.

Initial Conditions

A uniform discretization of the computational plane was employed such that computational nodes were coincident with the available experimental points (see Fig. 2) and were twice as dense. For the drag experiments, this resulted in 19 nodes in the interval $-1.5 \leq Y/D \leq 0.0$ and 31 nodes in the interval $-1.5 \leq Z/D \leq 1.0$. Triangular sub-domains were used which resulted in 1080 finite elements. In the simulation for the self-propelled experiments the right hand boundary was extended to $Y/D = 1.5$ and the above grid was reflected into the right half plane, thus doubling the number of elements.

The drag calculation was initialized by placing the experimental values of the mean velocity components \bar{U} , \bar{V} , and \bar{W} and the turbulence kinetic energy,

$$K = \frac{1}{2} (\overline{u'u'} + \overline{v'v'} + \overline{w'w'}) ,$$

directly on the appropriate nodes. In the second quadrant of Fig. 2 the intermediate nodes were initialized by simple $X - Y$ interpolation. In the third quadrant $R - \theta$ interpolation was used.

The initialization of the isotropic dissipation function deserves special mention. Ideally this experimentally unmeasured quantity should be initialized to be consistent with the stress model, Eqs. (8) through (10). Experience has shown that this works very well for two-dimensional flows where ϵ may be determined, for example, from the solution of Eq. (9) using the leading term on the right hand side. However, using this procedure for three-dimensional flows will result in a different solution for each of the model equations thus illustrating the deficiencies of an isotropic eddy viscosity model. Some pre-processing of the experimental data using the described turbulence model revealed that in addition the measured shear stresses were often inconsistent with the signs of the mean velocity gradients. For these reasons a different initialization procedure for the turbulence dissipation was employed. The dissipation was assumed to related to the turbulence kinetic energy through a dissipation length scale,

$$l_d = \frac{K^{3/2}}{\epsilon} . \quad (13)$$

Numerical experiments were conducted to determine a value of l_d which would cause the computed characteristic values of shear to be similar to the data. A value of $0.20D$ was selected. The dissipation function was then initialized from Eq. (13). The initial stress distributions are then prescribed by Eqs. (5) through (10). Figures 3a and 3b are

illustrative of the results of the procedure connecting the isotropic dissipation function and the stresses. The vectors represent the resultant of the two principal shear stresses for the drag-body wake in the plane $X/D = 0.042$, where τ_x is defined by

$$\tau_x \equiv \frac{1}{U_\infty^2} ((\overline{u'v'})^2 + (\overline{u'w'})^2)^{1/2}.$$

The data show that the stress is generally well correlated with the velocity gradient in this instance. The near wake is approximately axisymmetric downstream of the cylindrical slender body. In this region the stress is dominated by the radial component and $\tau_x \propto -\partial \overline{U}/\partial R$ where R is measured outward from the body centerline. Downstream of the strut the velocity deficit is considerably weaker and nearly two-dimensional. The data show small non-zero values of $\overline{u'v'}$ at the vertical symmetry line $Y/D = 0.0$. Figure 3b is a plot of the stress vectors as derived from Eqs. (8) and (9) and the experimental (interpolated) data for the mean velocity components and the normal stresses. There is good agreement, both qualitatively and quantitatively, between the experimental measurements and the modeled values.

Typical initial distributions ($X/D = 0.042$) for the axial velocity and turbulence kinetic energy produced by these procedures are shown in Fig. 4. The near-wake velocity profile for the drag body is nearly axisymmetric in the lower portion with a maximum velocity deficit of about 80% at the body centerline. The strut wake is nearly two-dimensional with a maximum deficit of 20%. The highest levels of kinetic energy are located about one-quarter body diameter from the centerline and in the wake of the strut.

Identical procedures were employed to initialize the computation of the self-propelled experiment. Figure 5, for example, is the initial swirl velocity ($X/D = 0.208$),

$$V_s \equiv \frac{1}{U_\infty} (\overline{V}^2 + \overline{W}^2)^{1/2},$$

as it was interpolated for the self-propelled experiment. The data were interpolated onto the left-half computational plane and the right-half plane was initialized by reflecting the dependent variables symmetrically or anti-symmetrically as appropriate. This procedure is not rigorously justified for the self-propelled calculation since the vertical plane $Y/D = 0.0$ is not a plane of symmetry for this flow. Unfortunately virtually no data is available for the fluid properties in the right-half plane. The small number of measurements taken, however, show approximate symmetry still exists at the near-wake plane $X/D = 0.208$. The next section will discuss the results of the calculations for both the drag and self-propelled conditions.

4. RESULTS AND COMPARISON WITH EXPERIMENTAL DATA

Drag-Body Wake

For purposes of comparing the calculations with the experiments it was found to be more illustrative to compare along radials in the flow field as defined by the angle θ in Fig. 2. This was done because of the large amount of interpolation necessary to contour the experimental data which was obtained on an increasingly irregular grid. However, it is worthwhile to present several contour plots in order to expose the general characteristics of the computations.

Figures 6a and 6b are contour plots of the computed axial velocity and the turbulence kinetic energy respectively at $X/D = 33.0$ downstream of the drag body. In the far wake the maximum velocity deficit has decreased to about 9% of the freestream velocity and has moved upward from the body centerline by a small amount. This is in accord with the experiments and is due to the disparity in diffusion rates between axisymmetric and two-dimensional wakes. The maximum turbulence is located radially at about $R/D = 0.3$ at $\theta = 150^\circ$. Turbulence levels in the wake of the strut are considerably lower. Figure 7a shows the axial decay of turbulence as characterized by the maximum value of K anywhere in the flow field, K_m , the value at the body centerline, $K_c = K(X/D, 0, 0)$, and the value at the strut centerline, $K_s = K(X/D, 0, 1)$. Also shown are the data for each of the measuring stations and generally the agreement is excellent. The favorable comparison between the calculation and experiment for the centerline K at $X/D = 33.0$ may be somewhat fortuitous since the calculation at $X/D = 1.0$ is not in agreement. Given the high radial gradients in both the mean velocity and turbulent energy in the near wake, it is reasonable to anticipate that somewhere in the early wake there does exist a developmental region wherein the production of turbulence is high, similar to that shown in Fig. 7a. That the data show essentially identical values of K_c at both $X/D = 1.0$ and $X/D = 33.0$ suggests that this mixing region is downstream of $X/D = 1.0$ and the calculation has simply overpredicted the rate of mixing. Clearly the geometry of the trailing edge will have considerable influence on the location and extent of the developmental region. Chevray (1968) presents data showing the centerline turbulence intensities increasing until $X/D = 0.5$ downstream of a body of revolution. Merz et al. (1986) show the intensities beginning to decay by $X/D = 0.3$ in the wake of a semielliptical afterbody. Schetz and Jakubowski (1975) show the maximum turbulence levels to increase until $X/D = 10.0$ and the centerline values to increase until about $X/D = 5.0$ in the wake downstream of a pointed stern model similar to that used in these experiments.

Figure 7b shows the longitudinal development of axial velocity as characterized by the maximum velocity existing anywhere in the flow field, \overline{U}_m , the value at the body centerline, \overline{U}_c , and the value at the strut centerline midway between the upper and lower bodies, \overline{U}_s . The agreement between the prediction and the data is excellent. The effect of non-zero $\partial P_c/\partial X$ in the early wake is evident by comparing with the zero pressure gradient solution given by the dotted lines. Figures 8a through 8c show the Reynolds stresses at $X/D = 33.0$. The slight upward migration of the body wake is observable in these figures.

As stated earlier detailed comparisons between the calculation and the experiment are more clearly performed by displaying the results along radials as defined by the angle θ in Fig. 2. Figures 9 and 10 compare the computed and measured distribution of mean velocity and turbulence kinetic energy along the 90° , 135° , and 180° radials. The simulation, of course, is coincident with the experiment at $X/D = 0.042$ since these were the initial conditions. In general the calculation is in good qualitative agreement with the data. The predicted velocity near the wake center is slightly high at $X/D = 1.0$ and slightly low at $X/D = 33.0$. The predicted values for $R/D \geq 0.3$ are almost coincident with the data. The dotted lines at $X/D = 1.0$ and $X/D = 33.0$ in Fig. 9a show the effect of neglecting the measured axial pressure gradient in the near-wake region.

The kinetic energy computation in Fig. 10 is in excellent agreement with experiment along all radials at $X/D = 33.0$. At $X/D = 1.0$ and for $R/D > 0.20$ there is also excellent agreement. The discrepancy near the wake center discussed above with regard to Fig. 7 is evident. The calculation seems reasonable in that gradient diffusion has enhanced the turbulence near the centerline. The region near $R/D = 0.1$ in the plane $X/D = 1.0$ is one of high shear and high velocity gradients. The production term in Eq. (11) is locally high compared to the dissipation, although the latter may have been initialized at unrealistically low levels via Eq. (13). There results a region near $X/D = 1.0$ where the kinetic energy increases with streamwise distance before beginning to decay. The underpredicted levels of K along the 90° radial in the outer portion of the wake at $X/D = 1.0$ are a result of a combination of the initial dissipation level and the application of the boundary conditions. The axial velocity was required to have zero gradient normal to this plane. The computed and measured velocity gradients along this radial were also small. Since the transverse velocities are also of little consequence in this flow, the turbulence production term is very small in the early wake along this radial. As shown in Fig. 4 the turbulence level, and also the dissipation through Eq. (13), was initially high and relatively uniform along $Y/D = 0.0$. The result of all of this is that the only term of consequence on the right hand side of

Eq. (11) at small X/D is the dissipation term which serves to nearly uniformly reduce the turbulence.

Figures 11a through 11d are plots of the computed Reynolds shear stresses along various radials at the three experimental data planes. In these figures the computational initial conditions at $X/D = 0.042$ are not coincident with the experimental data. The stresses are not computed via transport equations but rather are determined from the constitutive relations Eqs. (5) through (10). As discussed previously, only one length scale is permitted by the model and the value $l_d = 0.2D$ was selected to preserve the characteristic magnitude of the data. The figures show that the initialization technique resulted in a very good qualitative representation of the data for all stresses along all radials at $X/D = 0.042$. Some stresses along some radials are initialized slightly high in magnitude and some are initialized slightly low. The streamwise evolutions of the different stresses are in general agreement with the data. The calculation underpredicts the decay rate by a small amount between the first two data planes. The magnitudes and spatial distribution of the calculated stresses and the data are in good agreement at $X/D = 33.0$.

The experimentally measured transverse velocities at the three data planes for the drag body are shown in Fig. 12. The data at $X/D = 0.042$ show some skewing of the flow and perhaps the onset of a vortex. They approximately reflect the anticipated behavior that the axisymmetric body wake should entrain fluid radially and the strut wake should entrain fluid horizontally. At $X/D = 1.0$ the characteristic magnitude has fallen to about 3% of U_∞ and a well developed vortex is visible in the wake of the axisymmetric lower body. A weaker counter-rotating structure appears to be forming in the strut wake region. These structures are probably a consequence of slight model misalignment although the upper structure could be formed in the juncture region of the strut and the axisymmetric body. The data at $X/D = 33.0$ show an almost uniform skewing of the flow. This measurement location was very near the end of the wind tunnel test section and the wake development is likely influenced by the downstream effects.

Since the initial and boundary conditions are not known to the order of accuracy necessary to simulate this second order behavior, the measured transverse velocities were not used to initialize the computation for the drag-body experiments. Rather these velocity components were assumed to be equal to zero at the input plane and allowed to develop. Typical results are shown in Fig. 13. Figure 13a is the predicted transverse velocity distribution after several computational steps ($X/D = 0.05$). Very small entrainment velocities are predicted in the manner anticipated. The magnitude of this flow entrainment continues to increase until approximately $X/D = 0.2$ where the

maximum transverse velocity is nearly 0.5% of the freestream velocity. At $X/D = 1.0$ the maximum value has fallen to about 0.3% as shown in Fig. 13b.

Self-Propelled Wake

The fluctuating velocity field downstream of a propeller is composed of several components:

- 1) a periodic component at the blade revolution rate,
- 2) a component generated in the boundary layer over the blade,
- 3) a component generated across the shed vortex sheet and,
- 4) a component generated upstream of the propeller.

The first of these is not turbulence in the conventional sense and the evolution of this unsteady flow cannot be treated within the framework of the present model. Unfortunately the majority of the data available for the subject experiments (Mitra, Neu, and Schetz, (1986)) are point r.m.s. measurements and are contaminated by the periodic components. The limited spectral information available from the experiments is insufficient to selectively and consistently remove this component. For lack of a better alternative and with the realization that the numerical simulation thus loses a portion of its applicability, the experimental data were used without adjustment to initialize the calculation.

The shear stress data shown in Fig. 14a may exhibit some of the local contamination due to the periodic component. From consideration of the mean flow velocity gradient field alone, one expects the stress to be predominantly radial and opposed to the velocity gradient. This would result in two peaks of opposite sign in the wake of the axisymmetric body, with the stress directed toward the center in the innermost region and directed outward in the velocity overshoot region. The data of Fig. 14a approximate this behavior for $R/D \leq 0.4$. Beyond this radius the stress is predominantly circumferential. In Fig. 14b is plotted the resultant stress derived from Eqs. (8) and (9) with $l_d = 0.2D$ in Eq. (13). It is seen that the mean velocity data do not support a significant tangential component.

Figures 15a and 15b are plots of the streamwise velocity and turbulence kinetic energy distributions as interpolated onto the initial computational plane ($X/D = 0.208$). In the near wake the maximum velocity deficit is approximately 20% of the freestream velocity in the region downstream of the strut and about 70% downstream of the self-propelled body. Maximum velocity overshoots are about 10% at R/D near 0.5. Other than very close to the slender model centerline the turbulence kinetic energy decreases with increasing distance from the center until there are local spikes in the data at

$R/D \approx 0.5$. These are probably due to the unsteady vortex shedding discussed above and as such are not a true representation of the turbulence in the flow field.

The distributions shown in Figs. 14 and 15 along with the transverse velocity distribution of Fig. 5 were used to initialize the calculation at $X/D = 0.208$. Before making a detailed comparison of computation and experiment along selected radials, the contour plots of Figs. 16 and 17 serve as useful indicators of the overall characteristics of the numerical solution at the most downstream data plane ($X/D = 28.0$). At this cross-plane the velocity deficit downstream of the propeller hub has vanished completely. Velocities greater than freestream exist at all points in the plane downstream of the self-propelled model with peak velocity overshoots of about 3% of U_∞ still existing near $R/D = 0.5$. There is a remnant of the drag wake remaining in the region behind the strut. The contours in this area are elongated in a clock-wise manner due to the convective action of the swirling flow. The turbulence kinetic energy distribution shown in Fig. 16b also has this feature. The turbulence in the lower wake is maximum at the center and decreases with distance away from the center. The three components of Reynolds shear stress are shown in Fig. 17. In this case it is noted that the $\overline{v'w'}$ component is of the same order as the the other two components, an indication that the transverse gradients of all three velocity components are of the same order.

Figures 18 and 19 contrast the experimental and calculated swirl velocities at $X/D = 1.0$ and $X/D = 28.0$, respectively. Comparing with Fig. 5, the data show the swirl to have decreased only slightly between the first two stations. The calculation is in overall agreement but predicts somewhat greater decay of the swirl. At $X/D = 28.0$ the calculation is remarkably consistent with the data in terms of the maximum velocity level and the extent of radial spread. The data, however, show the swirl along any radial to peak in the vicinity of $R/D = 0.25$ whereas the calculation shows the peak values to occur in the vicinity of $R/D = 0.5$ to 0.75 .

Figure 20a shows the streamwise evolution of the turbulence kinetic energy as characterized by values at the centerlines of both the self-propelled body and the connecting strut. Again the far-wake turbulence levels are in very good agreement while the predicted near-wake velocity gradient production region is not evident in the data. The near-wake region on the other hand is very well reproduced in the calculation for the streamwise velocity as is observed in Fig. 20b. Only the maximum velocity at $X/D = 1.0$ is significantly missed by solution. It should be pointed out that the value plotted at $X/D = 1.0$ is an isolated experimental datum along the 135° radial and that the average of the maximum values along the remaining radials is much closer to the computed curve. In the far wake all three characteristic velocities are slightly under-predicted. Note that in contrast to the drag-body experiment (Fig. 7b) the velocity

along the lower body centerline, \overline{U}_c , is eventually greater than that along the strut centerline.

Figures 21a through 21c compare the calculated and measured streamwise velocity along the 90° , 135° , and 180° radials respectively. Generally the agreement is good. The numerical solution consistently overpredicts the diffusion for small R/D for each of the radials with the discrepancy being greatest along 90° . The simulation is consistently very good beyond $R/D = 0.3$. Note that the maximum overshoot velocity is very well predicted along the 90° and 180° radials and only along the 135° radial, as mentioned above, is there a significant deviation.

Figures 22a through 22c compare the computed and measured K distributions along the same three radials considered above. The peaks in the initial data ($X/D = 0.208$) near the propeller tips are evident. To the extent that the data are contaminated by the periodic component, the comparison with experiment is not meaningful in this region. As explained above, the calculation was initialized with these data for lack of any consistent alternative. These unrealistic stress levels, however, do not seriously infect the numerical solution for the following reason. The isotropic dissipation function, initialized by Eq. (13), was also correspondingly high. The region near $R/D = 0.5$ is one of very low swirl velocity (Fig. 5) and very small radial velocity gradients (Fig. 21). The convection and production terms in Eqs. (11) and (12) are therefore locally negligible in the early wake and the spikes in the distributions are quickly diffused and dissipated. This action is observed in Fig. 22 between the first two stations. The turbulence level at $X/D = 28.0$ is well predicted along all three radials. The local minimum between $0.5 \leq R/D \leq 0.75$ along the 90° radial is due to the swirl flow convection (see Fig. 16b) and is not evident in the data.

The curves of Fig. 23 are typical of any of the shear stress components along any radial. The derived values at $X/D = 0.208$ qualitatively represent the data with the exception of some localized data points. The data show the stresses in some cases to be of greater magnitude at $X/D = 1.0$ than at $X/D = 0.208$ whereas the computation shows a continuous decay. The shear stresses have essentially vanished by $X/D = 28.0$.

5. SUMMARY

The calculation and experiment for the drag wake are in good overall agreement. Gross features of the flow such as the far-wake magnitudes of certain characteristic mean velocities and turbulence parameters are in excellent agreement. It should be noted that the imposition of the experimental axial pressure gradient is essential to obtain the level of agreement reported insofar as the streamwise velocity is concerned.

This gradient appears to be imposed in the experiment from the surrounding potential flow field.

Detailed comparisons of the planar distributions of the measured and calculated streamwise velocity also show very good agreement along all radials for both downstream data planes. The computed planar distribution of turbulence kinetic energy essentially interpolates the data distribution in the far-wake plane. In the plane $X/D = 1.0$ the calculated turbulence is in good agreement with the data except for very small R/D near the slender body centerline, and large R/D along the $\theta = 90^\circ$ radial. Some of this discrepancy is undoubtedly due to unrealistic initial distribution of the isotropic dissipation function in these regions of small to vanishing Reynolds shear stress. Some of the discrepancy near the wake center is possibly more apparent than real given the sparseness of the axial distribution of data planes which may have prevented the observation of some details predicted by the computation. Slight mismatches in axial position can produce large differences as indicated by the calculations.

The Reynolds shear stresses, which are not dependent variables of the computation, are shown to be reasonably well simulated by the constitutive model for the drag-wake experiment. Correct magnitudes are predicted in the far wake and qualitatively similar distributions for both data and calculation exist throughout the computational domain.

The calculation of the self-propelled wake does not agree as favorably with the experiment in certain localized details such as the turbulence kinetic energy and Reynolds shear stresses near the propeller blade tips. A significant amount of the discrepancy is possibly due to the presence of periodic components in the data.

Significant "rolling" of the strut wake due to propeller swirl is predicted but not evident in the data possibly because of the absence of measurements in the first and fourth quadrants.

The predicted swirl flow velocities agree in magnitude with the data although there is some variance with regard to the location of the maxima along radials in the plane.

The evolutions of certain characteristic mean flow velocities and turbulence levels are again in good overall agreement with the data. The notable exception is the prediction of significant near-wake turbulence production which was not observed in the experiment.

The results show that generally satisfactory predictions can be obtained without any swirl specific modifications to the K, ϵ turbulence model. This is not to imply that such modifications are unnecessary. Any attempt, however, to identify and rectify

defects in the model will likely be frustrated unless comprehensive experimental data for all flow properties at several closely-spaced downstream planes become available.

6. ACKNOWLEDGEMENTS

The author acknowledges the support of the Office of Naval Research (Code 12) and the Naval Research Laboratory for Cray computer computational support, and particularly wishes to thank Dr. E. W. Miner for his assistance in pre-processing the experimental data and displaying the computed results.

7. REFERENCES

- Baker, A.J., Manhardt, P.D., and Orzechowski, J.A., (1979), "A Numerical Solution Algorithm for Prediction of Turbulent Aerodynamic Corner Flows," AIAA Paper No. 79-0073.
- Baker, A.J., (1983), *Finite Element Computational Fluid Mechanics*, McGraw-Hill/Hemisphere, New York.
- Chevray, R., (1968), "The Turbulent Wake of a Body of Revolution," J. of Basic Engineering, Vol. 90, pp. 275-284.
- Gesner, F.B. and Emery A.F., (1976), "A Reynolds Stress Model for Turbulent Corner Flows, I: Development of the Model," J. of Fluids Engineering, Trans. ASME, pp. 261-268.
- Hanjalic, K. and Launder, B.E., (1972), "A Reynolds Stress Model of Turbulence and its Application to Thin Shear Flows," J. Fluid Mechanics, Vol. 52, Pt. 4, pp. 609-638.
- Launder, B.E. and Ying, W.M., (1973), "Prediction of Flow and Heat Transfer in Ducts of Square Cross-Section," Proc. Institution of Mechanical Engineers, Vol. 187, pp. 455-461.
- Merz, R.A., Yi, C.H., and Przirembel, C.E.H., (1986), "Turbulence Intensities in the Near-Wake of a Semielliptical Afterbody," AIAA J., Vol. 24, No. 12, pp. 2038-2040.
- Mitra, P.S., Neu, W.L., and Schetz, J.A., (1985), "Effect of a Free Surface on the Wake of a Slender Body," VPI-Aero-146, Virginia Polytechnic Institute and State University, Blacksburg, Va.
- Mitra, P.S., Neu, W.L., and Schetz, J.A., (1986), "Effect of a Free Surface on the Wake of a Self-Propelled Slender Body," VPI-Aero-153, Virginia Polytechnic Institute and State University, Blacksburg, Va.
- Schetz, J.A. and Favin S., (1977), "Numerical Solution for the Near Wake of a Body with Propeller," J. of Hydronautics, Vol. 11, pp. 136-141.
- Schetz, J.A. and Favin S., (1979), "Numerical Solution of a Body-Propeller Combination including Swirl and Comparisons with Data," J. of Hydronautics, Vol. 13, pp. 46-51.
- Schetz, J.A. and Jakubowski, A.K., (1975), "Experimental Studies of the Turbulent Wake Behind Self-Propelled Slender Bodies," AIAA J. Vol. 13, pp. 1568-1575.
- Swanson, R.C. and Schetz, J.A., (1975), "Calculations of the Turbulent Wake Behind Slender Self-propelled Bodies with a Kinetic Energy Method," J. of Hydronautics, Vol. 9, pp. 78-80.

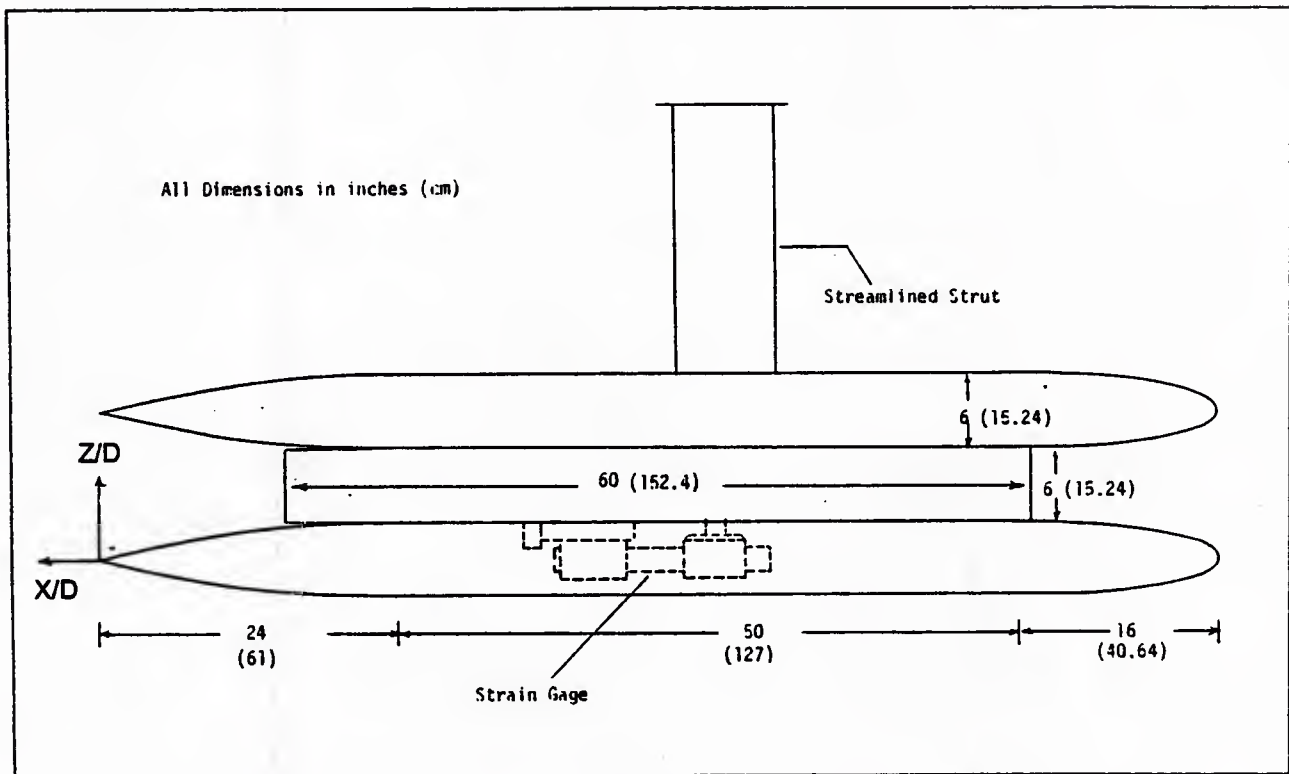


Fig. 1—Schematic of the experimental model

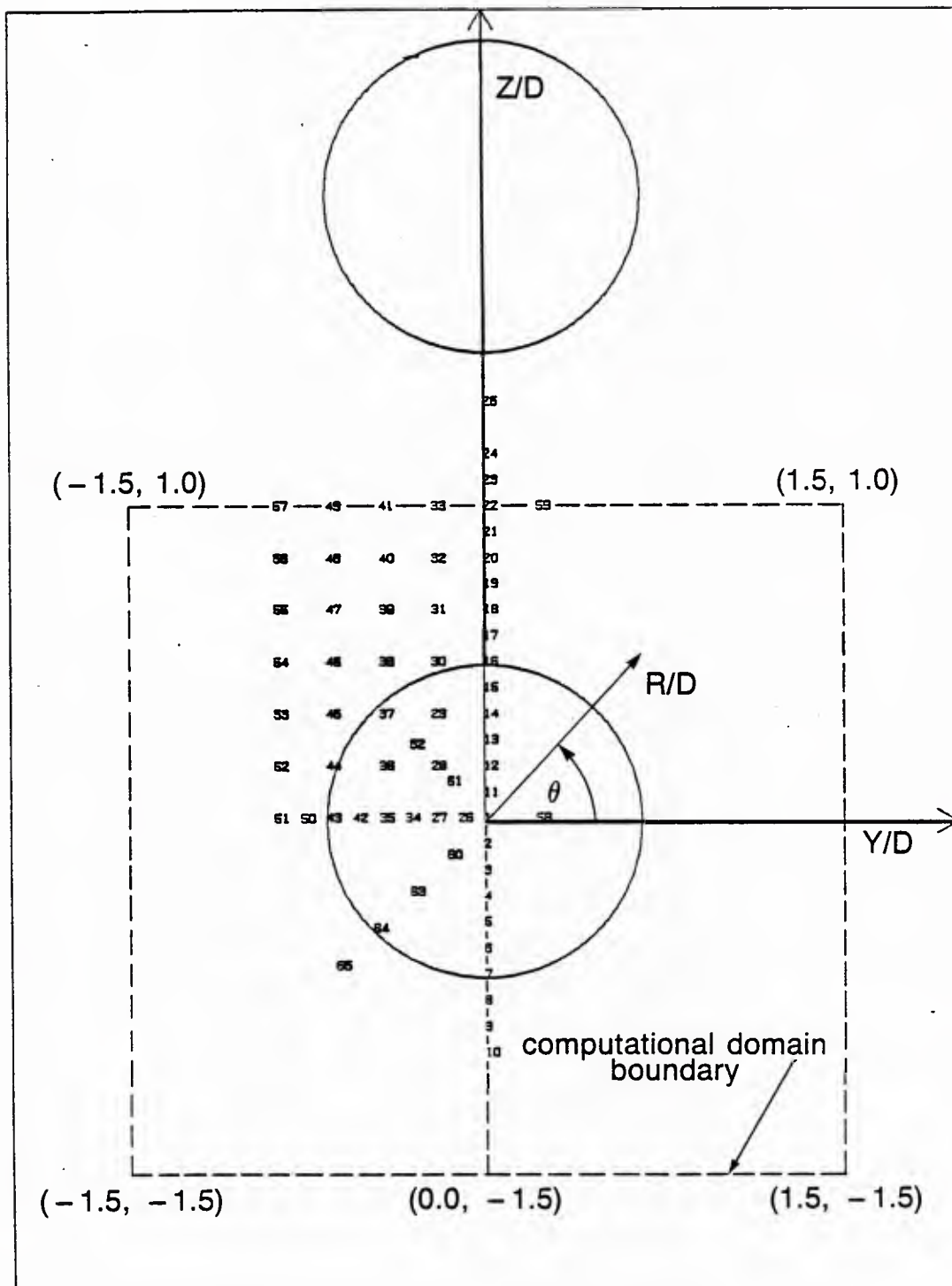


Fig. 2—Schematic of the experimental and computational domains of the $Y - Z$ plane

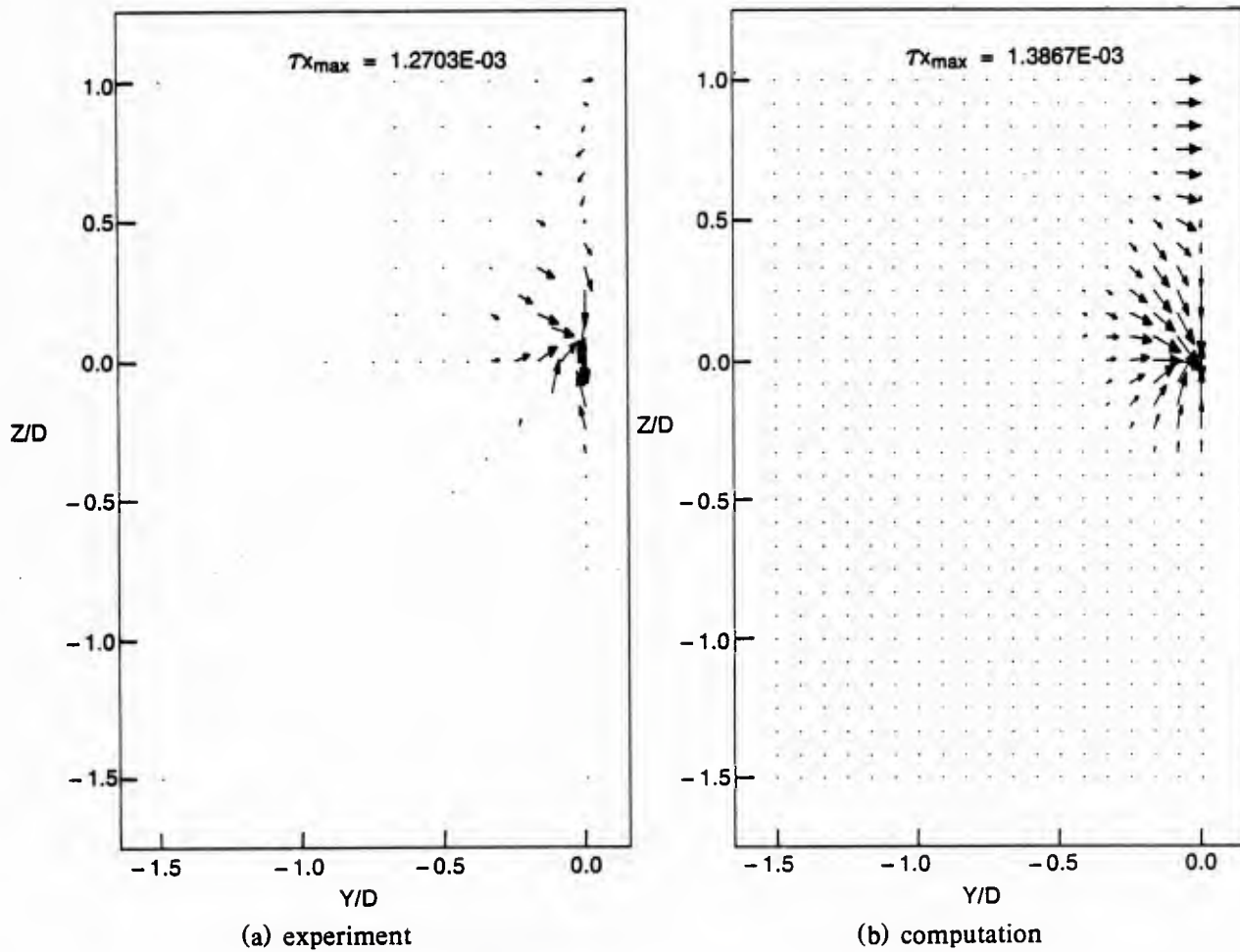
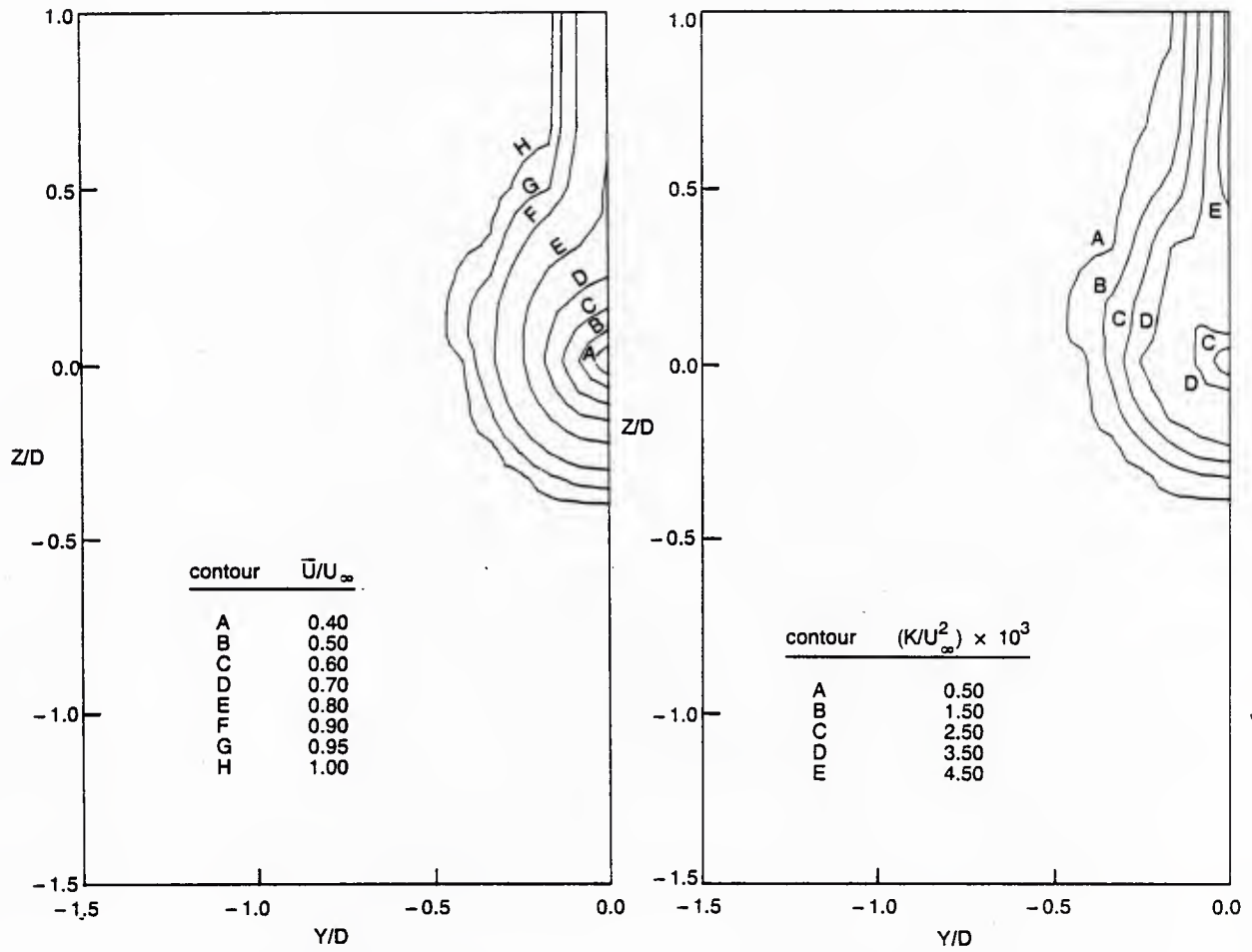


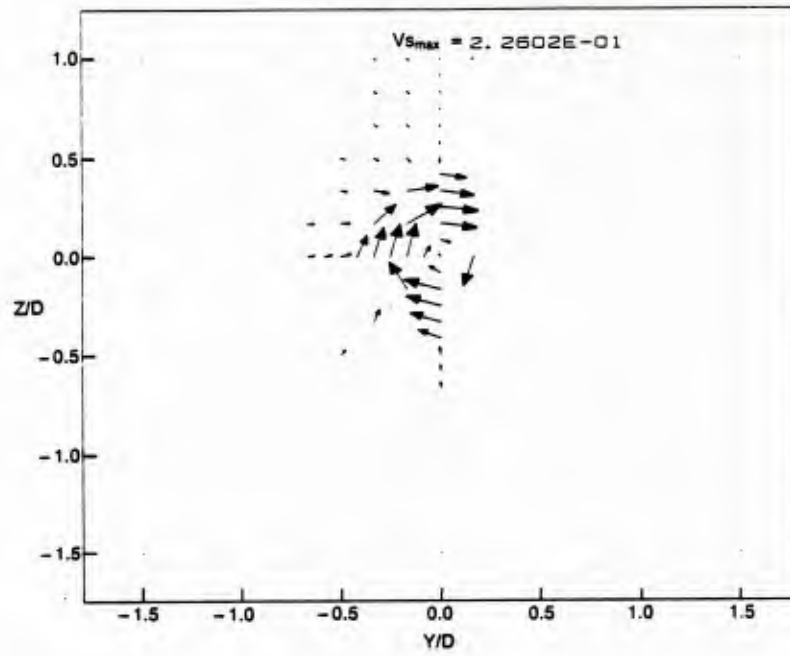
Fig. 3—Reynolds stress at $X/D = 0.042$ in the drag wake



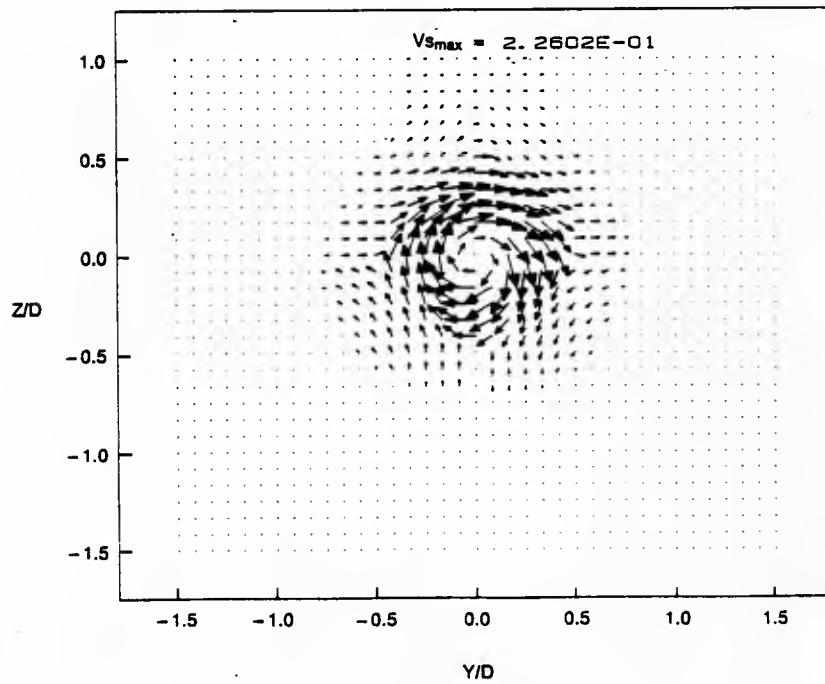
(a) mean streamwise velocity

(b) turbulence kinetic energy

Fig. 4—Initial conditions to computation at $X/D = 0.042$ in the drag wake

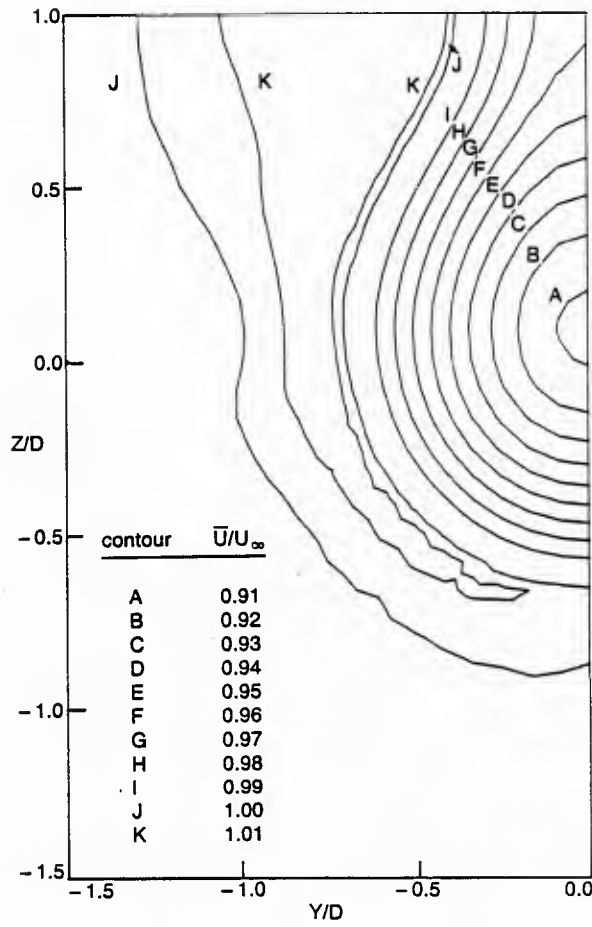


(a) experiment

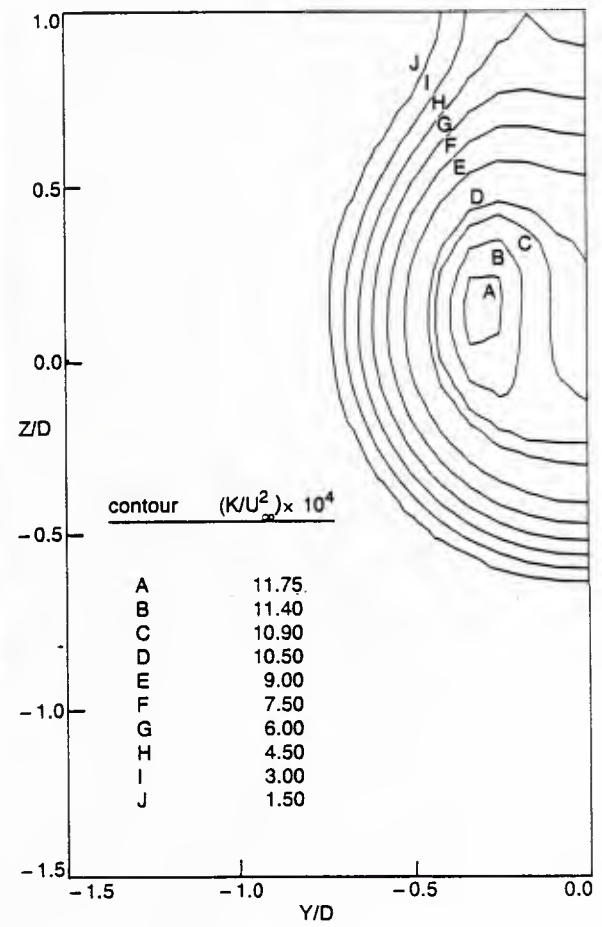


(b) computation

Fig. 5—Swirl velocity at $X/D = 0.208$ in the self-propelled wake

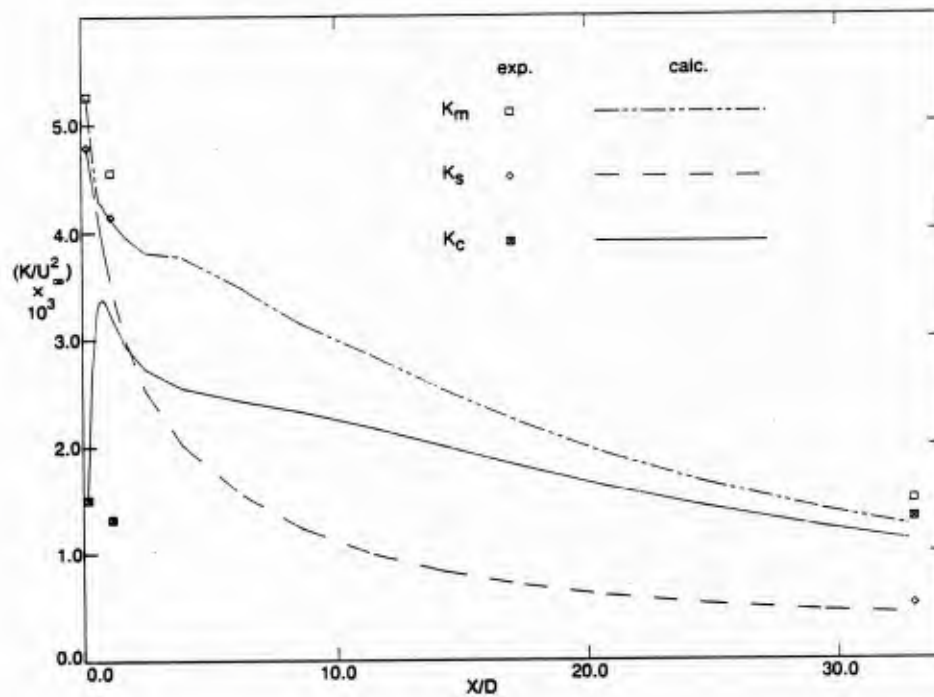


(a) streamwise velocity

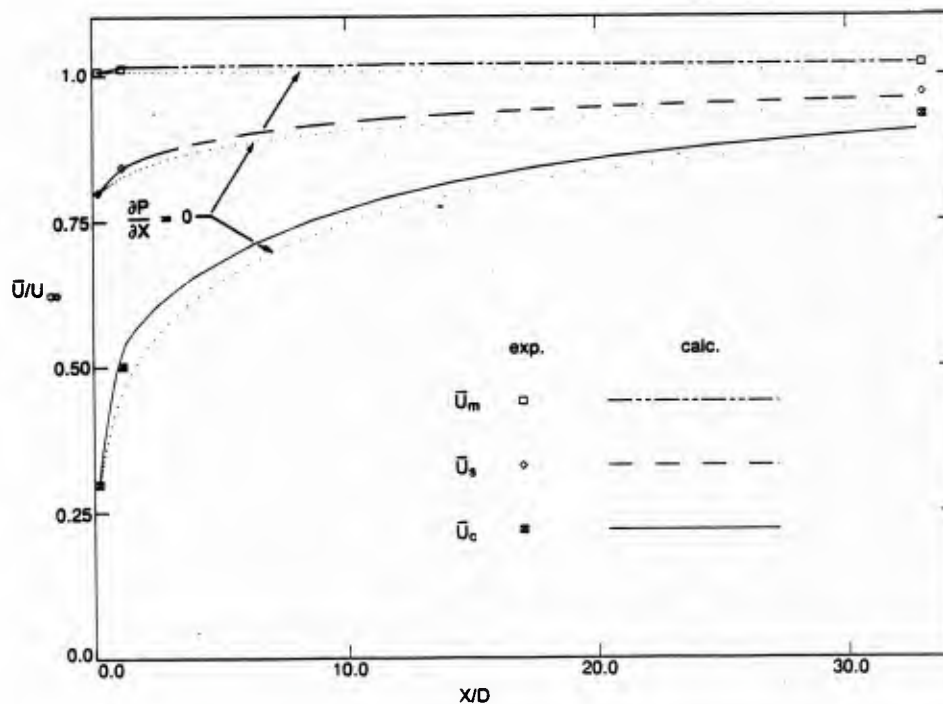


(b) turbulence kinetic energy

Fig. 6—Computed distributions of streamwise velocity and turbulence kinetic energy at $X/D = 33.0$ in the drag wake

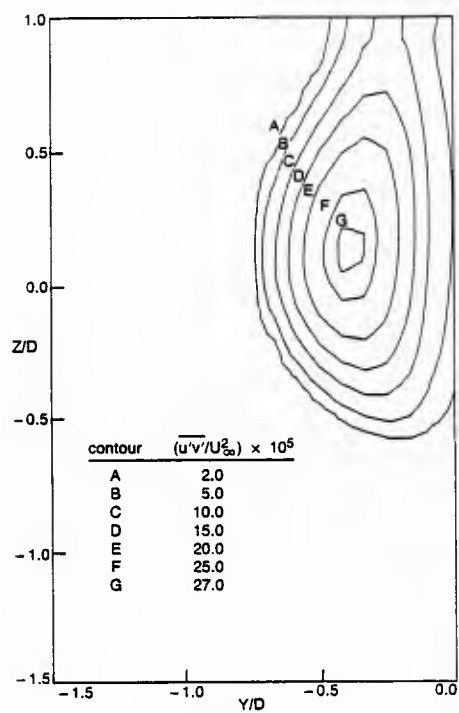


(a) turbulence kinetic energy

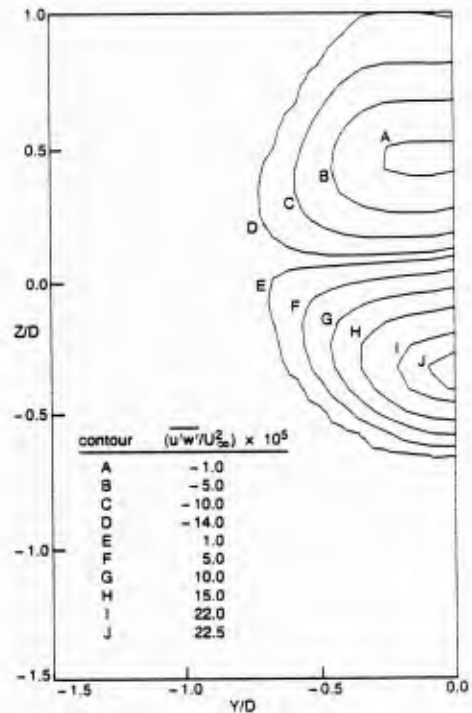


(b) streamwise velocity

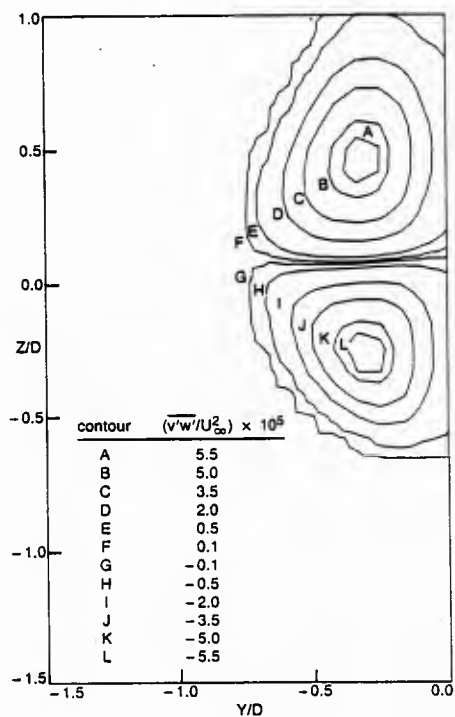
Fig. 7—Streamwise variation of characteristic values of turbulence kinetic energy and streamwise velocity in the drag wake.



(a) $\overline{u'v'}$



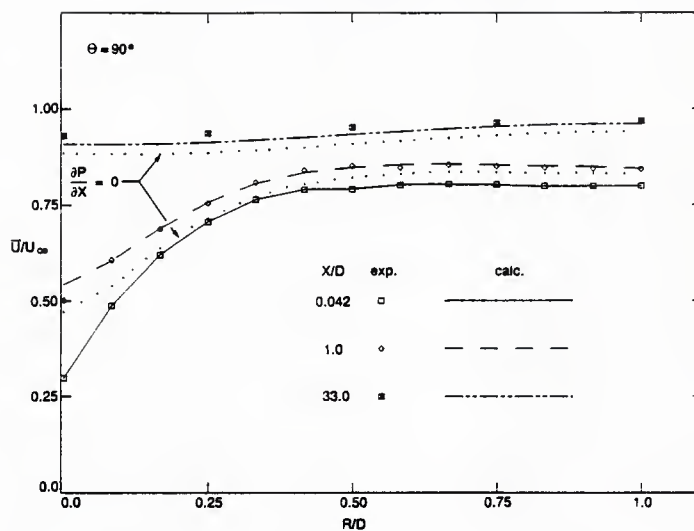
(b) $\overline{u'w'}$



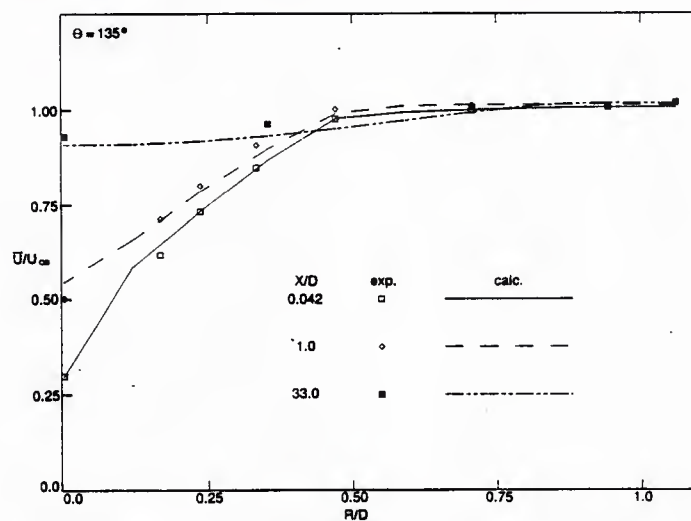
(c) $\overline{v'w'}$

Fig. 8—Computed distributions of Reynolds stresses at $X/D = 33.0$ in the drag wake

(a) $\theta = 90^\circ$



(b) $\theta = 135^\circ$



(c) $\theta = 180^\circ$

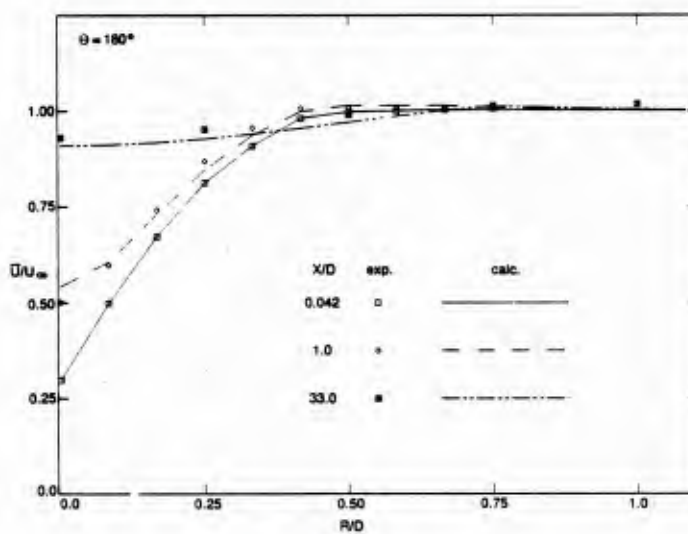
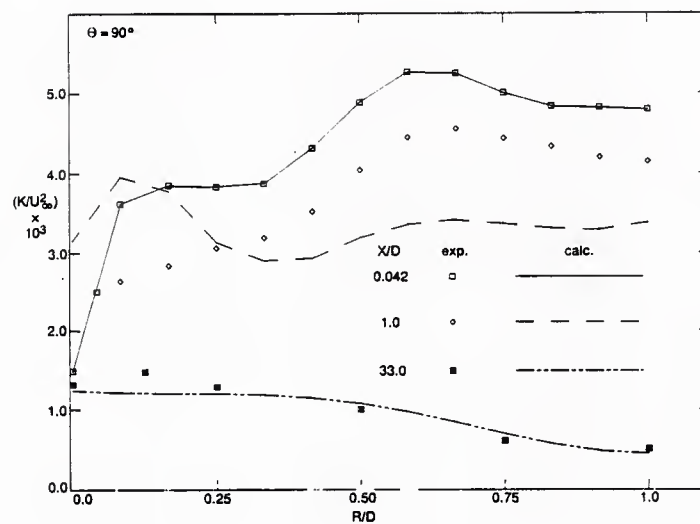
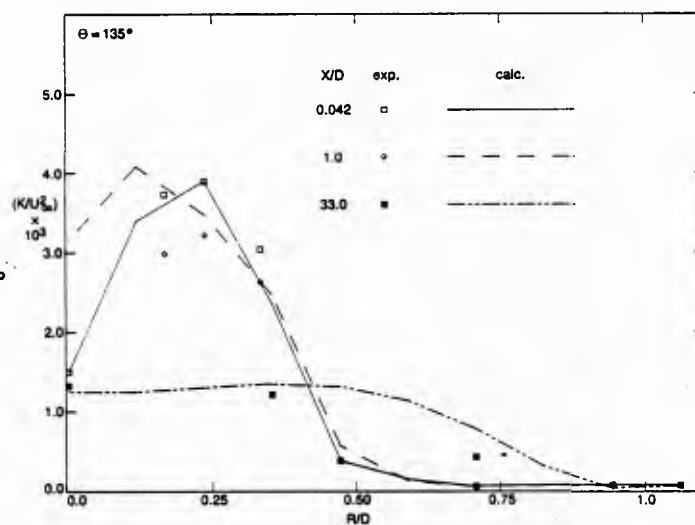


Fig. 9—Comparison of computed and measured steamwise mean velocity along selected radials in the drag wake

(a) $\theta = 90^\circ$



(b) $\theta = 135^\circ$



(c) $\theta = 180^\circ$

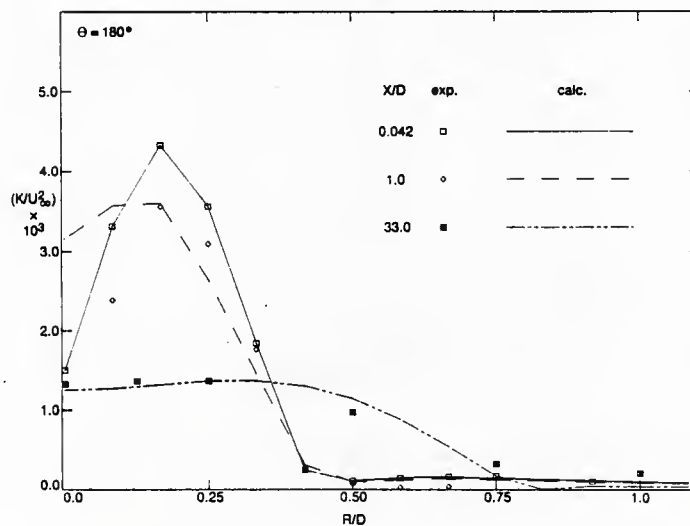
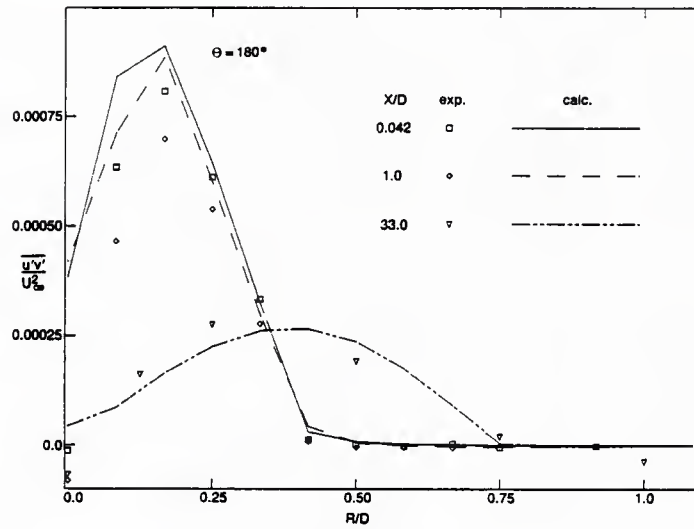
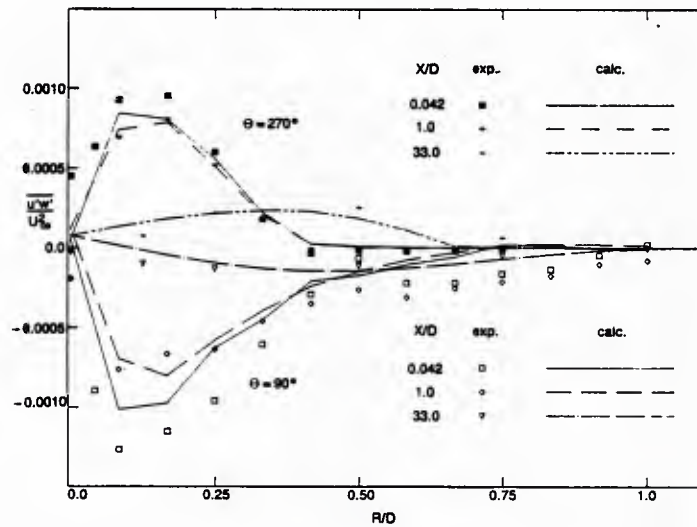


Fig. 10—Comparison of computed and measured turbulence kinetic energy along selected radials in the drag wake

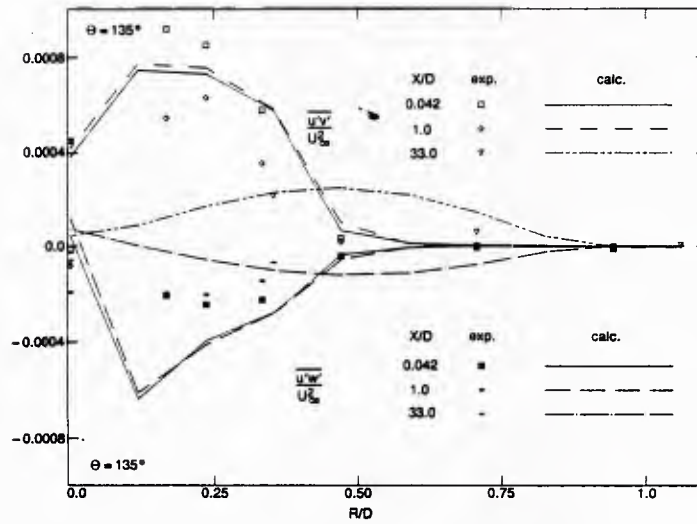


(a) $\overline{u'v'}; \theta = 180^\circ$

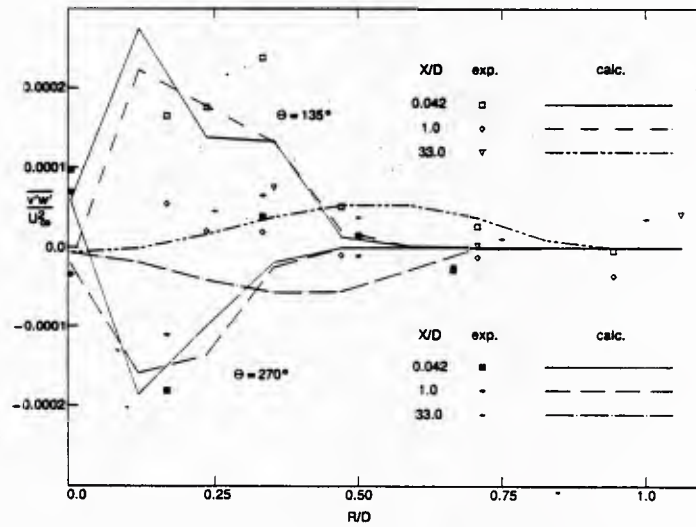


(b) $\overline{u'w'}; \theta = 270^\circ$ (upper), $\theta = 90^\circ$ (lower)

Fig. 11—Comparison of computed and measured Reynolds stresses in the drag wake

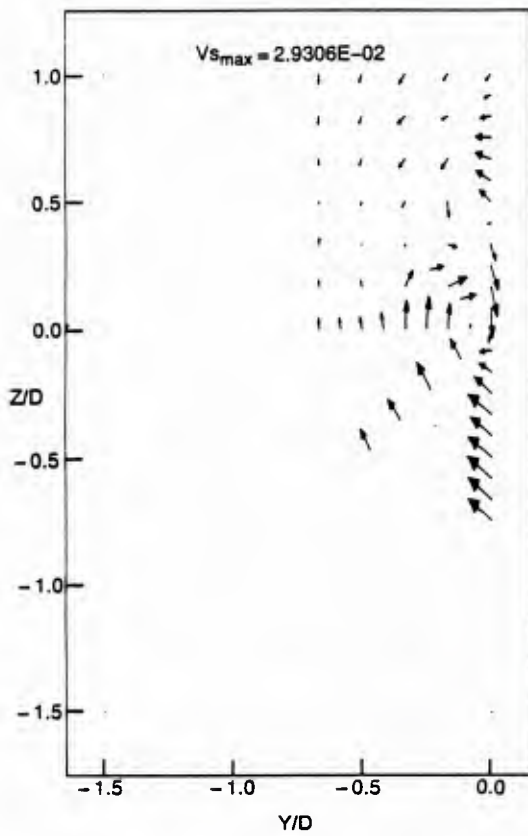


(c) $\overline{u'v'}$ (upper), $\overline{u'w'}$ (lower); $\theta = 135^\circ$

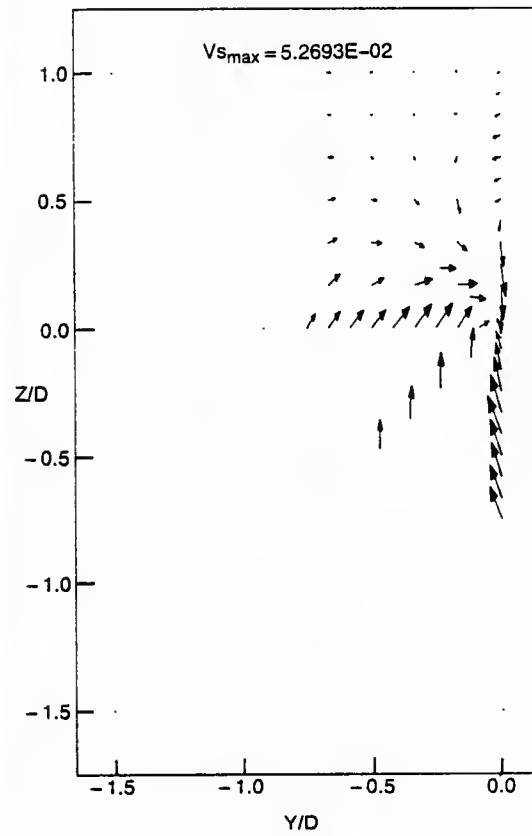


(d) $\overline{v'w'}$; $\theta = 135^\circ$ (upper), $\theta = 270^\circ$ (lower)

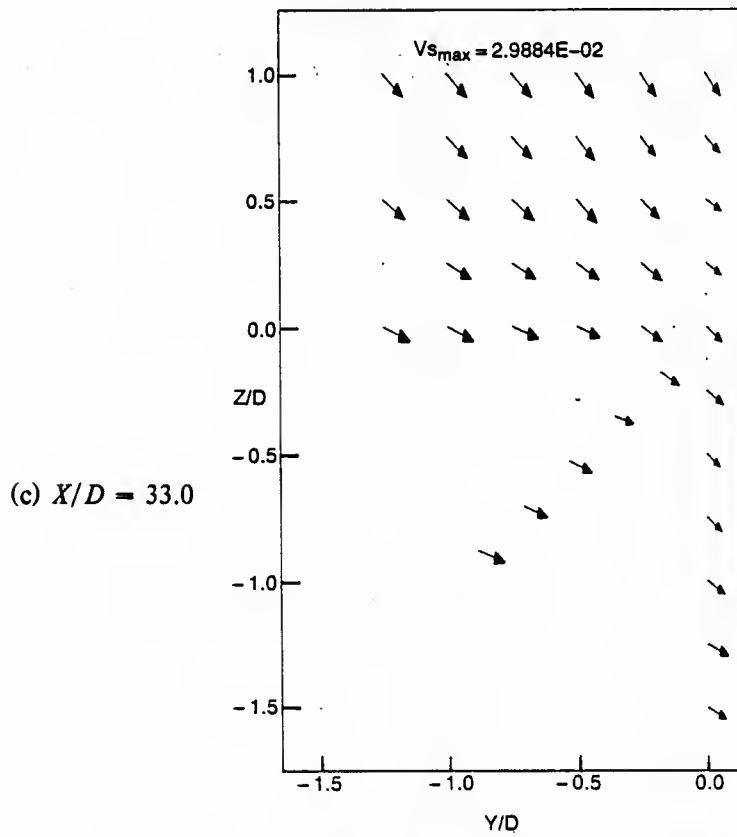
Fig. 11 (Continued) — Comparison of computed and measured Reynolds stresses in the drag wake



(a) $X/D = 0.042$

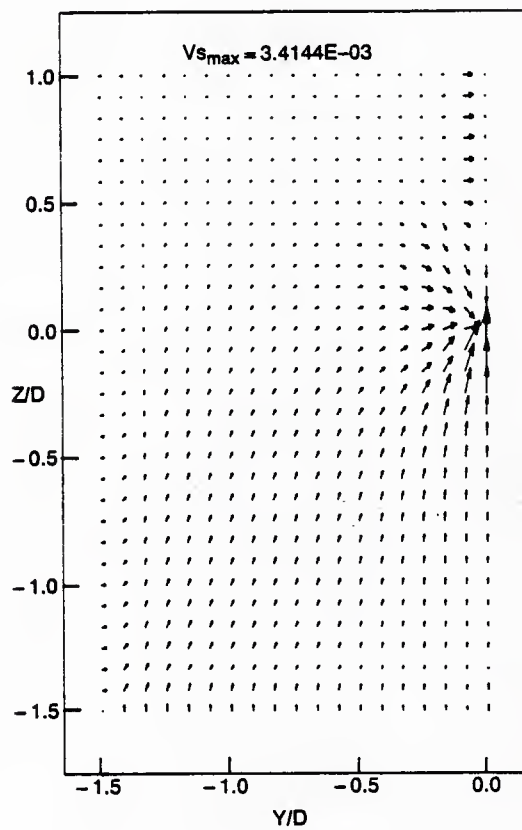


(b) $X/D = 1.0$

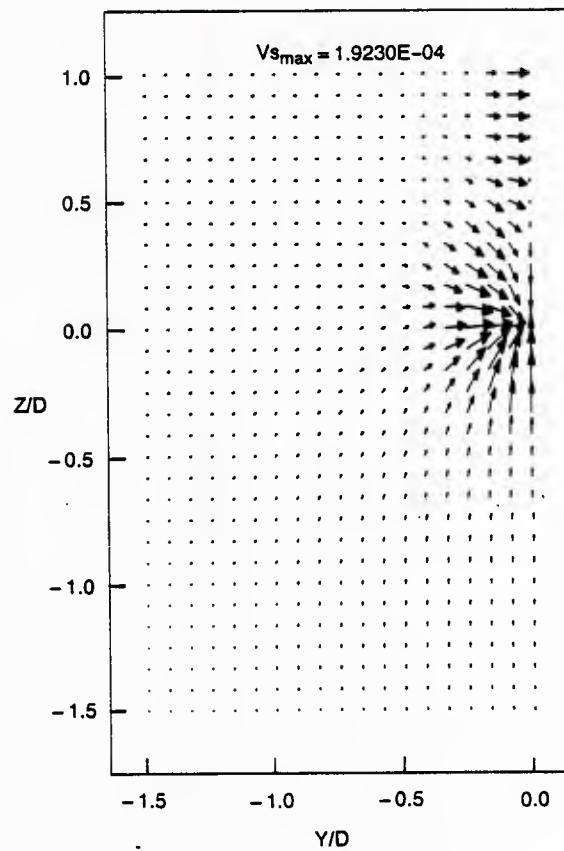


(c) $X/D = 33.0$

Fig. 12—Experimental secondary flow velocity vectors at the three data planes for the drag wake

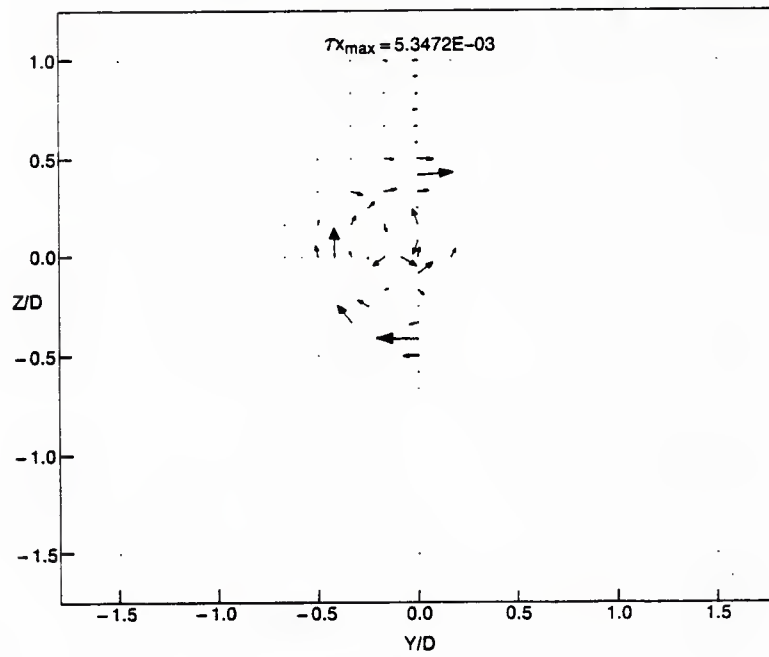


(a) $X/D = 0.05$

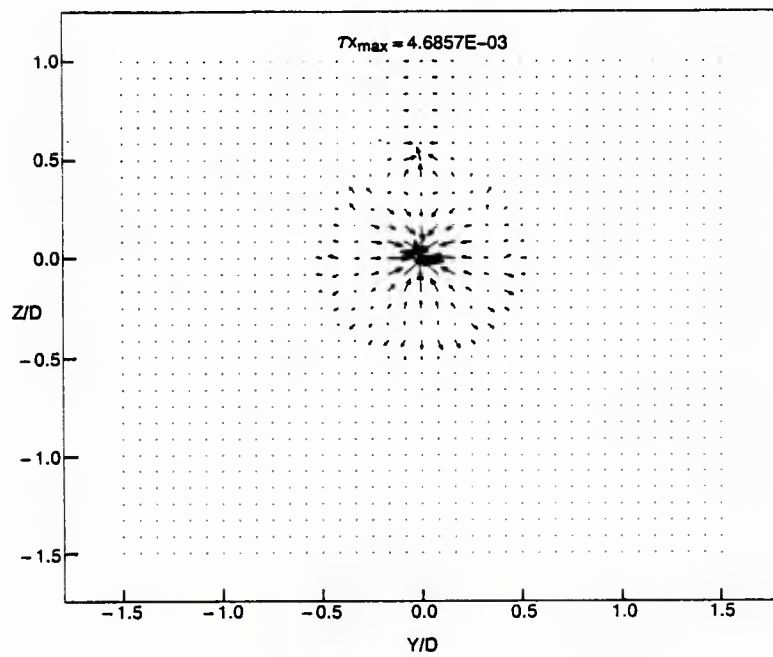


(b) $X/D = 1.0$

Fig. 13—Computed secondary flow velocity vectors in the near wake of the drag body

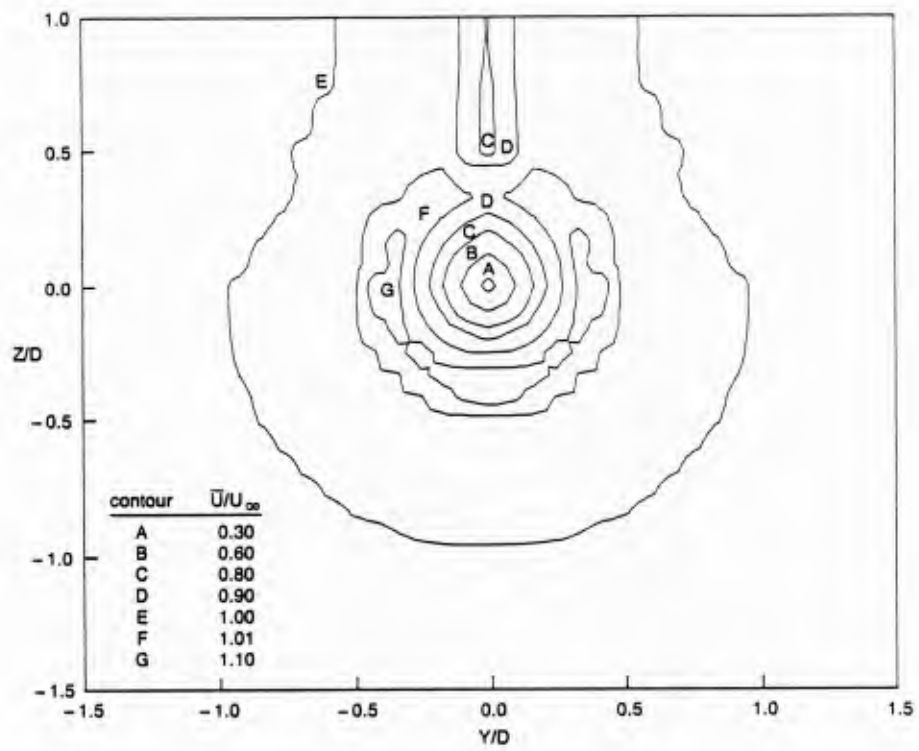


(a) experiment

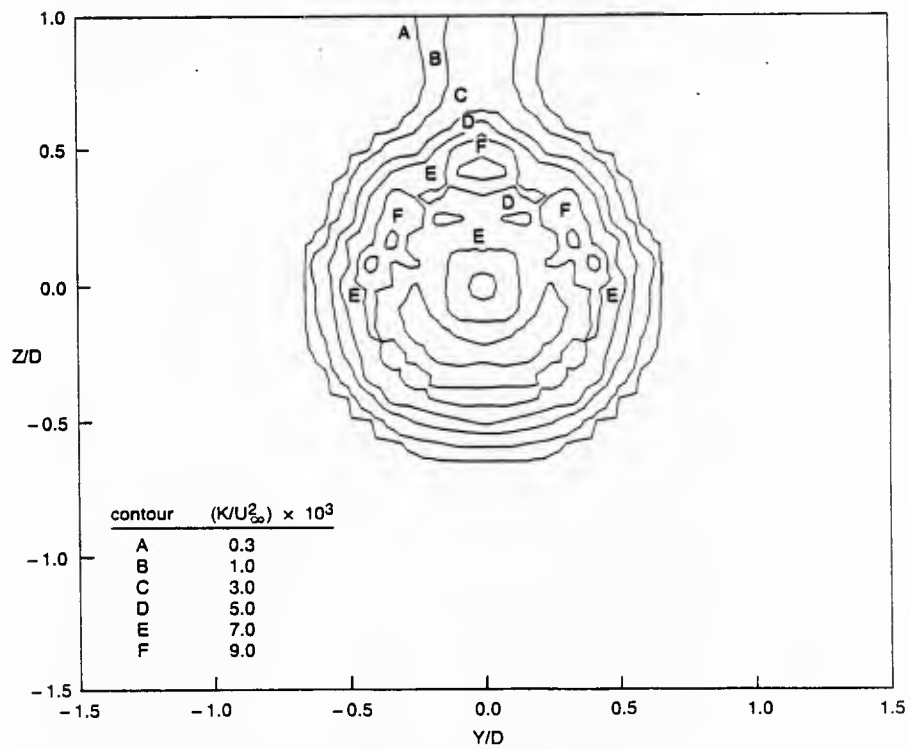


(b) computation

Fig. 14—Reynolds stress at $X/D = 0.208$ in the self-propelled wake

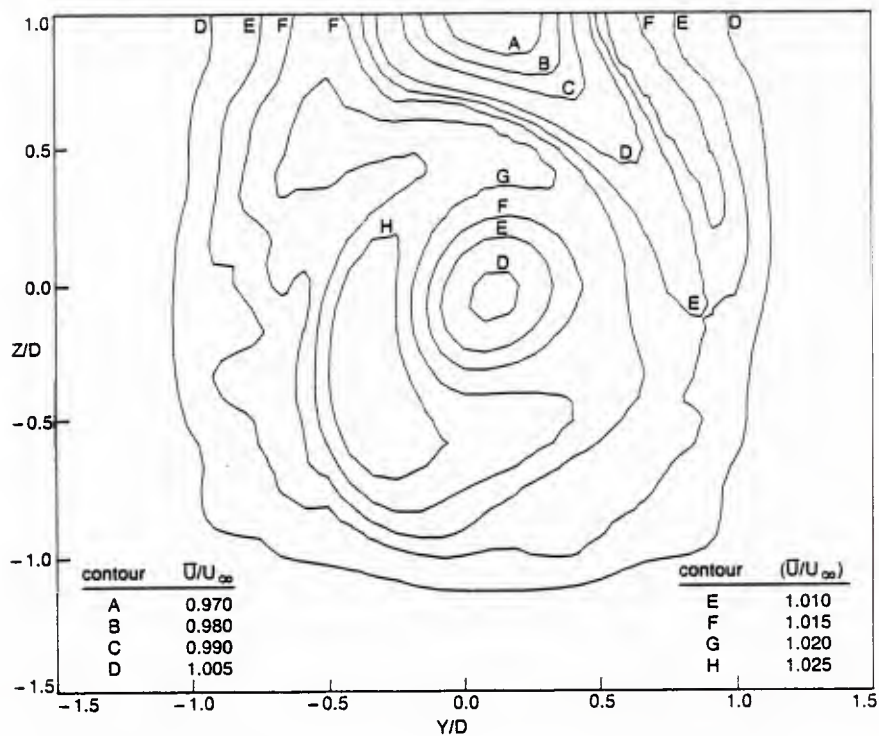


(a) mean streamwise velocity

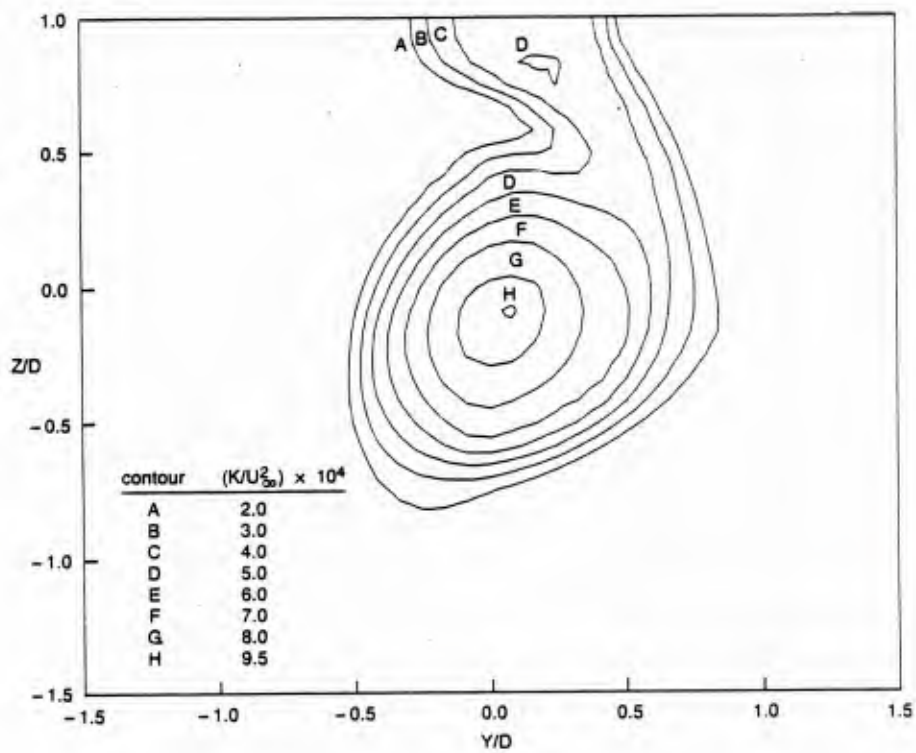


(b) turbulence kinetic energy

Fig. 15—Initial conditions to computation at $X/D = 0.208$ in the self-propelled wake



(a) streamwise velocity



(b) turbulence kinetic energy

Fig. 16—Computed distributions of streamwise velocity and turbulence kinetic energy at $X/D = 28.0$ in the self-propelled wake

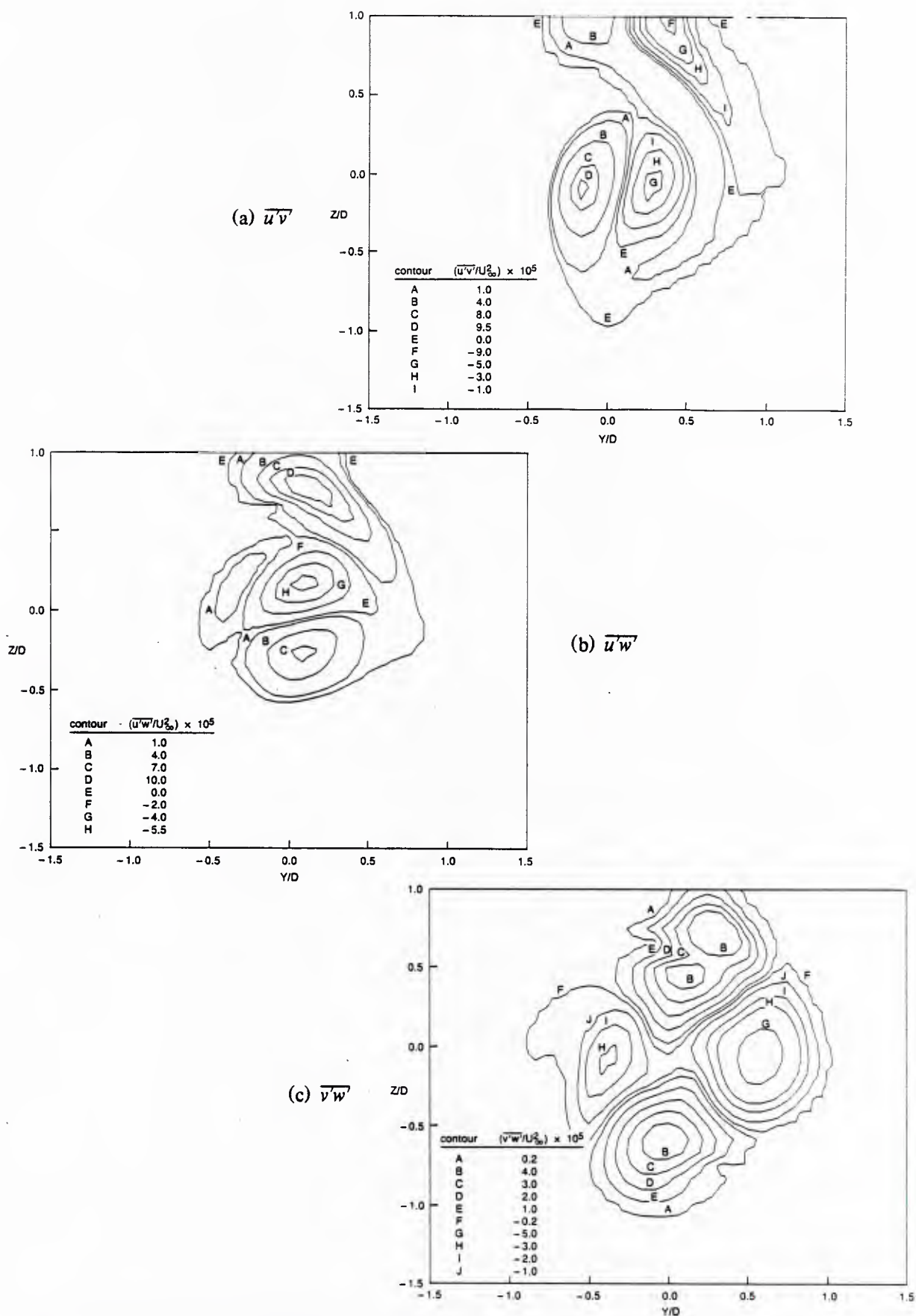
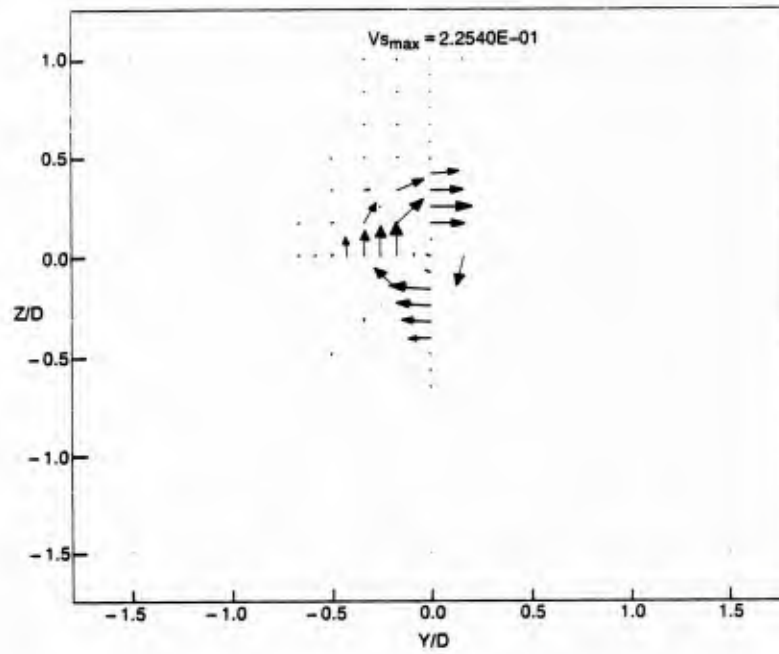
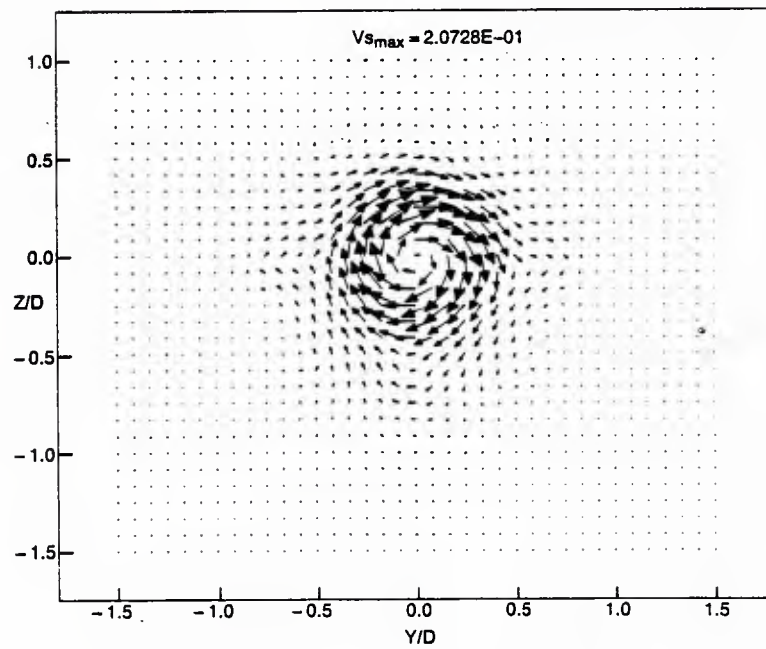


Fig. 17—Computed distributions of Reynolds stresses at $X/D = 28.0$ in the self-propelled wake

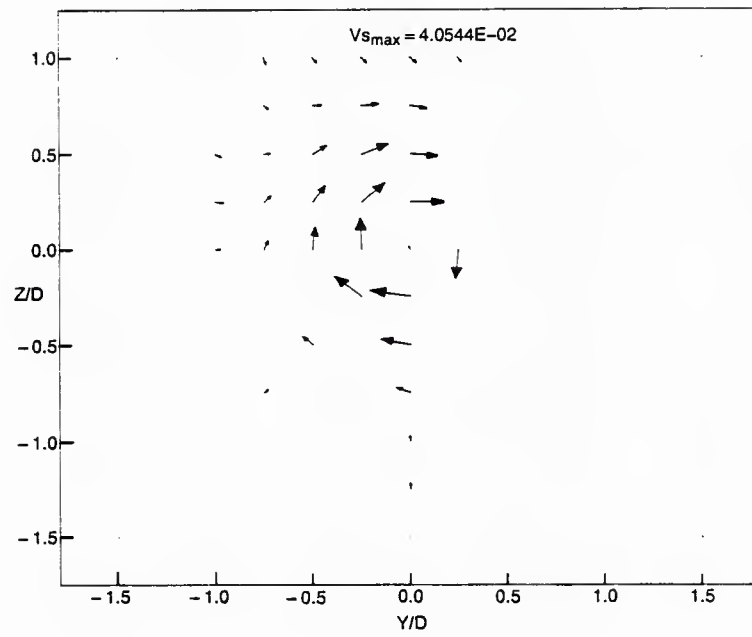


(a) experiment

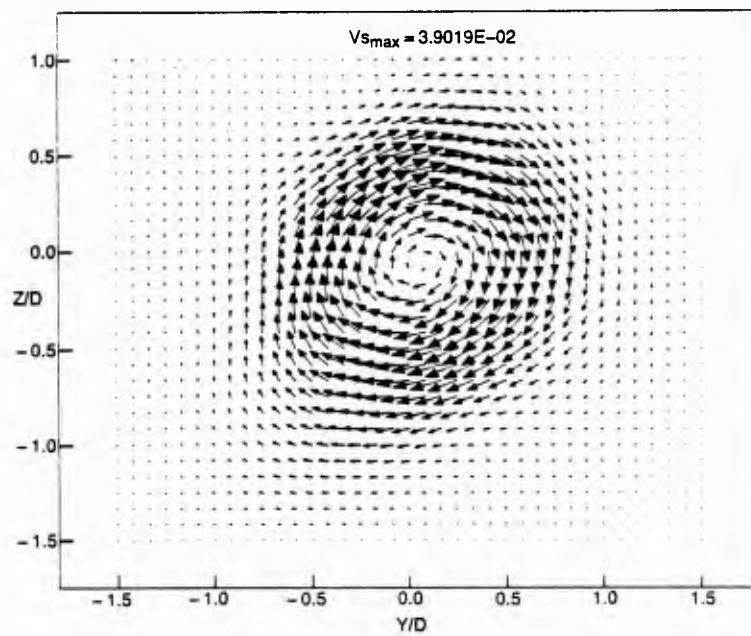


(b) computation

Fig. 18—Measured and computed swirl velocity vectors at $X/D = 1.0$ in the self-propelled wake

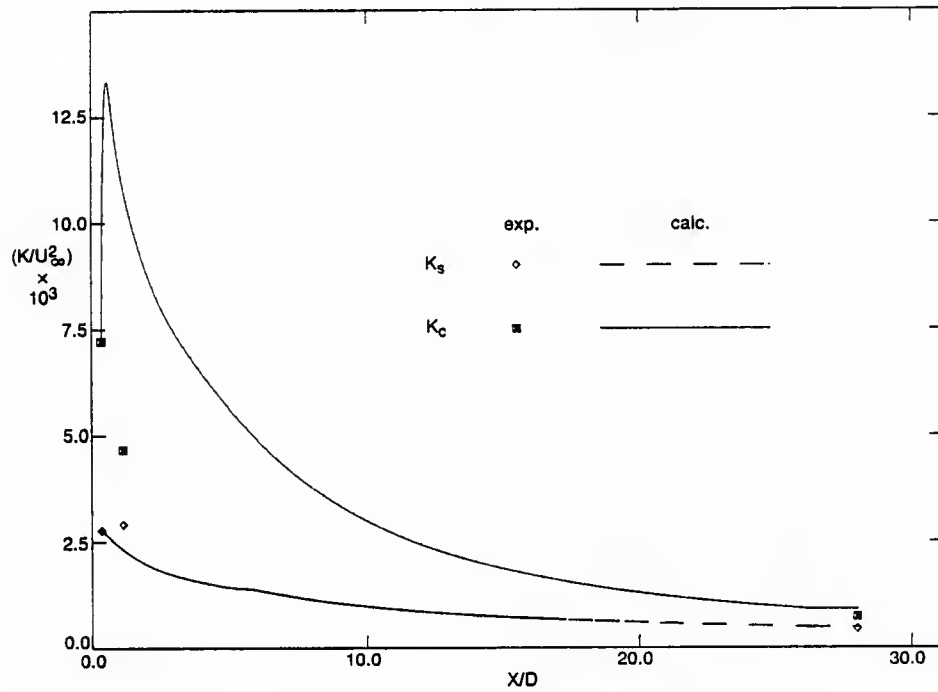


(a) experiment

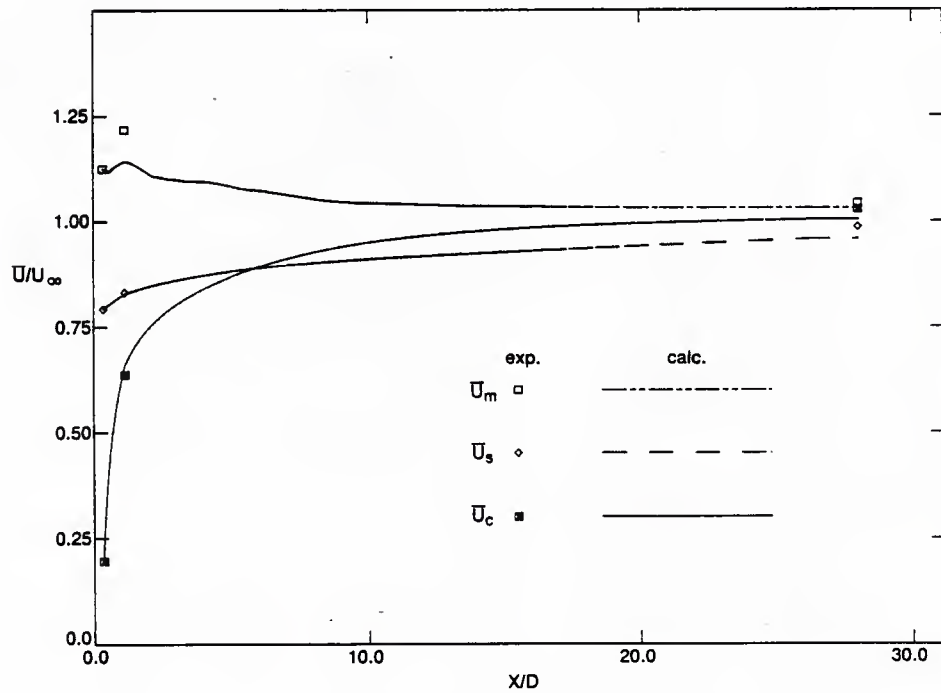


(b) computation

Fig. 19—Measured and computed swirl velocity vectors at $X/D = 28.0$ in the self-propelled wake

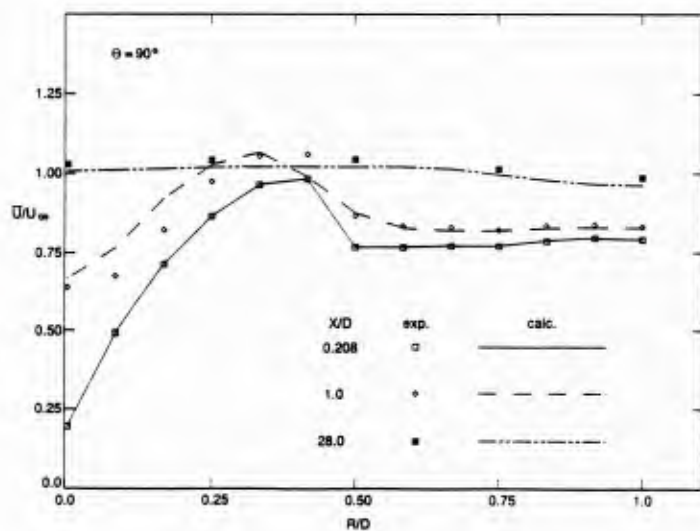


(a) turbulence kinetic energy

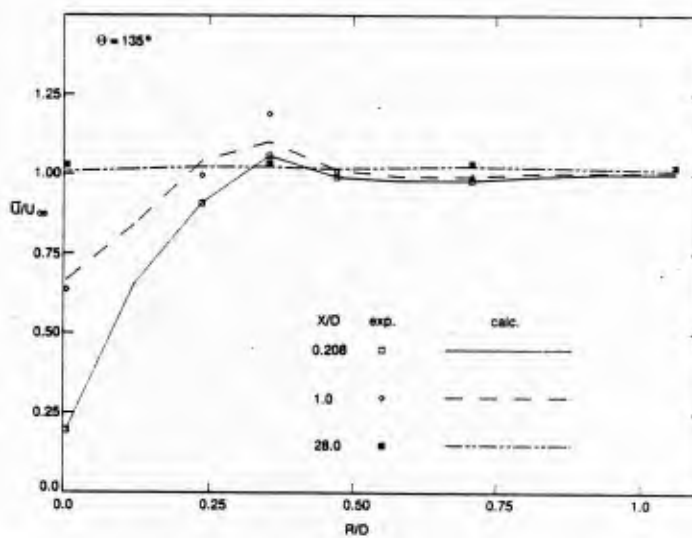


(b) streamwise velocity

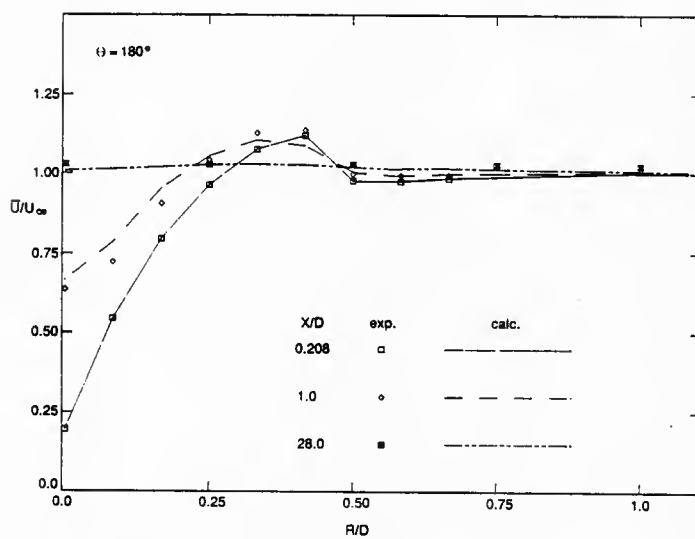
Fig. 20—Streamwise variation of characteristic values of turbulence kinetic energy and streamwise velocity in the self-propelled wake



(a) $\theta = 90^\circ$

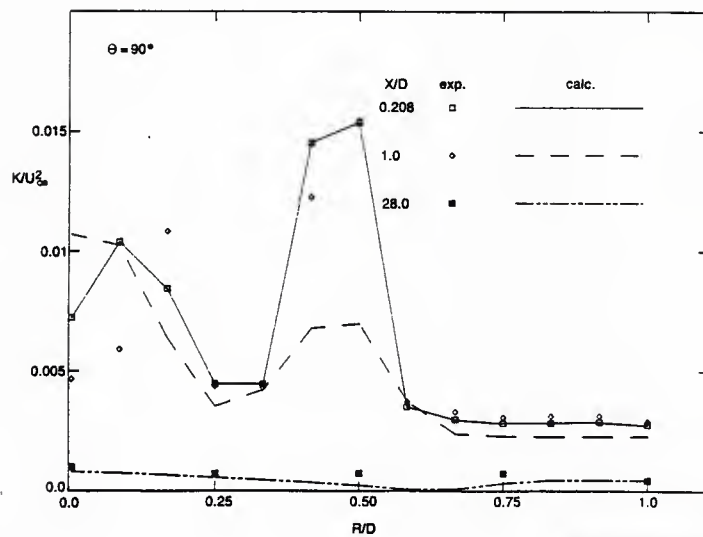


(b) $\theta = 135^\circ$



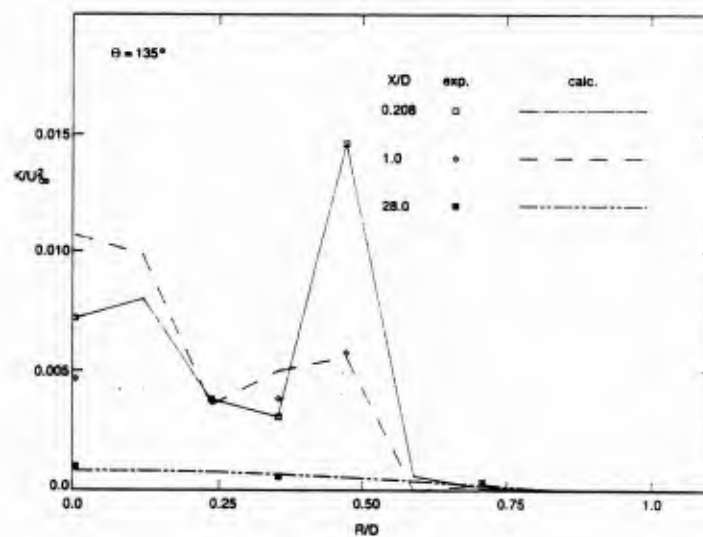
(c) $\theta = 180^\circ$

Fig. 21—Comparison of computed and measured streamwise mean velocity along selected radials in the self-propelled wake



(a) $\theta = 90^\circ$

(b) $\theta = 135^\circ$



(c) $\theta = 180^\circ$

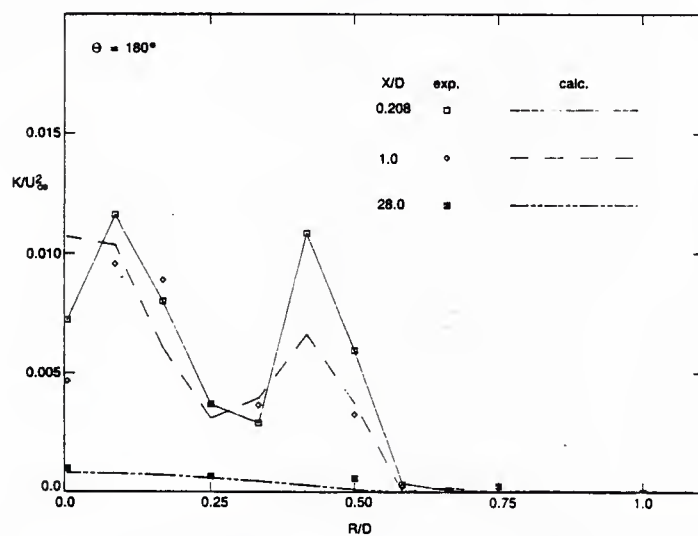
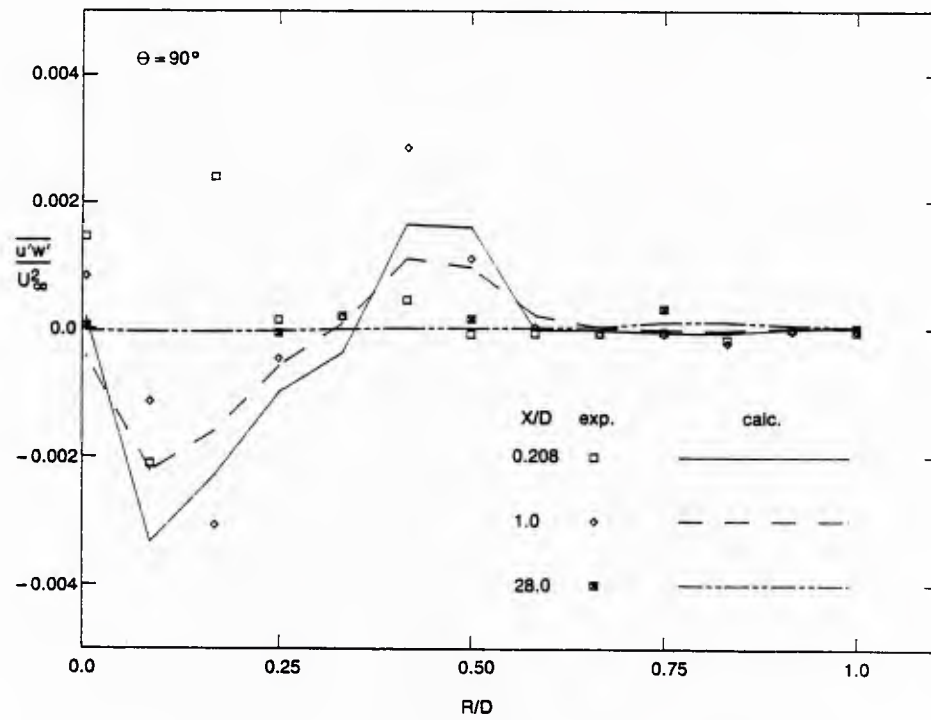
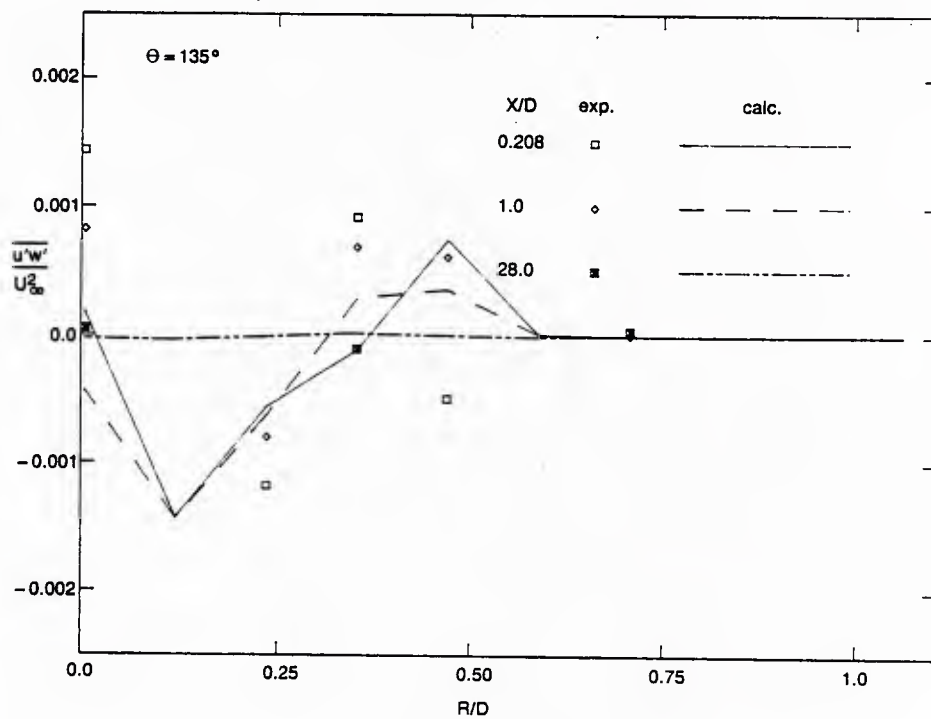


Fig. 22—Comparison of computed and measured turbulence kinetic energy along selected radials in the self-propelled wake



(a) $\overline{u'w'}; \theta = 90^\circ$



(b) $\overline{u'w'}; \theta = 135^\circ$

Fig. 23—Comparison of computed and measured Reynolds stress along selected radials in the self-propelled wake

U231220

DEPARTMENT OF THE NAVY

NAVAL RESEARCH LABORATORY
Washington, D.C. 20375-5000

OFFICIAL BUSINESS
PENALTY FOR PRIVATE USE, \$300

THIRD-CLASS MAIL
POSTAGE & FEES PAID
USN
PERMIT NO. G-9